

## CANCER

# Single-cell RNA sequencing highlights intratumor heterogeneity and intercellular network featured in adamantinomatous craniopharyngioma

Yu Jiang<sup>1†</sup>, Jinlong Yang<sup>1†</sup>, Ruichao Liang<sup>1†</sup>, Xin Zan<sup>1†</sup>, Rangrang Fan<sup>1</sup>, Baoyin Shan<sup>1</sup>, Hao Liu<sup>1</sup>, Li Li<sup>2</sup>, Yue Wang<sup>3</sup>, Min Wu<sup>4</sup>, Xin Qi<sup>1</sup>, Hongxu Chen<sup>1</sup>, Qingqing Ren<sup>1</sup>, Zhiyong Liu<sup>1</sup>, Yuelong Wang<sup>1</sup>, Jing Zhang<sup>1</sup>, Peizhi Zhou<sup>1</sup>, Qiang Li<sup>1</sup>, Meng Tian<sup>1</sup>, Jinhao Yang<sup>1</sup>, Chaoyang Wang<sup>1</sup>, Xueying Li<sup>1</sup>, Shu Jiang<sup>1</sup>, Liangxue Zhou<sup>1</sup>, Gao Zhang<sup>5\*</sup>, Yaohui Chen<sup>6\*</sup>, Jianguo Xu<sup>1\*</sup>

Copyright © 2023 The Authors, some rights reserved; exclusive licensee American Association for the Advancement of Science. No claim to original U.S. Government Works. Distributed under a Creative Commons Attribution NonCommercial License 4.0 (CC BY-NC).

Despite improvements in microscopically neurosurgical techniques made in recent years, the prognosis of adamantinomatous craniopharyngioma (ACP) is still unsatisfactory. Little is known about cellular atlas and biological features of ACP. Here, we carried out integrative analysis of 44,038 single-cell transcriptome profiles to characterize the landscape of intratumoral heterogeneity and tumor microenvironment (TME) in ACP. Four major neoplastic cell states with distinctive expression signatures were defined, which further revealed the histopathological features and elucidated unknown cellular atlas of ACP. Pseudotime analyses suggested potential evolutionary trajectories between specific neoplastic cell states. Notably, a distinct oligodendrocyte lineage was identified in ACP, which was associated with immunological infiltration and neural damage. In addition, we described a tumor-centric regulatory network based on intercellular communication in TME. Together, our findings represent a unique resource for deciphering tumor heterogeneity of ACP, which will improve clinical diagnosis and treatment strategies.

## INTRODUCTION

Adamantinomatous craniopharyngiomas (ACPs) are rare intracranial tumor that tend to occur in the sellar region and originates from embryonic malformation of the craniopharyngeal epithelium (a remnant of the ectoderm, also known as Rathke's pouch) (1, 2). Epidemiological statistics support a bimodal age distribution of patients with ACP, mainly in children aged 5 to 14 years and adults aged 50 to 74 years (2). Even extremely rare ACP cases occur in the prenatal and neonatal periods (3–5). ACPs are typically onset in childhood and adolescence and account for approximately 6 to 9% of pediatric brain tumors (6, 7). As the most common lesion involving the hypothalamic-pituitary axis in childhood, ACP causes catastrophic damage to endocrine homeostasis, growth, and development in patients (8, 9). Histopathologically, ACP is characterized by cysts, typically prominent calcifications and cholesterol crystals (2, 10). Finger-like protrusions of tumor epithelium form at the junction of tumor and normal tissue and invade surrounding important neural structures (6). This aggressive biological behavior makes treatment challenging and contributes to the poor prognosis (11). Surgery is still the first-line treatment for ACP. However, considering the aggressiveness of the tumor and the close relationship between the tumor and the position of the pituitary stalk, optic

chiasm, and especially hypothalamus, gross total resection is extremely challenging and often leads to serious neurological impairment and poor prognosis (12–14). Moreover, partial resection often causes frequent tumor recurrence (15). Therefore, surgery alone cannot solve the clinical problems caused by ACP, and it is necessary to develop a precision treatment that can effectively eliminate the tumor and reduce the damage to the surrounding normal structures. There is an urgent need for further in-depth understanding of the biological characteristics of ACP and the molecular mechanisms behind the origin and development of ACP.

Because of the lack of mature cell lines and organoid models, basic research on the tumor biology of ACP and its tumor microenvironment is progressing slowly. Previous studies supported the complex histological structure of ACP, while its cellular composition and functional characteristics are still unclear, which hinders our in-depth exploration of its tumorigenesis mechanism. Pathological staining can reveal the special internal organization of ACP, composed mainly of palisade-like epithelial cell layers, helical cell clusters, keratin nodules, and stellate reticulum (16, 17). This diversity of histological structures may lead to marked differences in cellular function. ACP is generally considered to be driven by mutations in exon 3 of the *Catenin Beta 1* (*CTNNB1*) gene (18–21). Activating mutations of *CTNNB1* prevent its encoded protein  $\beta$ -catenin from being degraded normally, leading to its accumulation in the nucleus and inducing persistent activation of the WNT pathway. Previous studies have suggested that the nuclear accumulation of  $\beta$ -catenin caused by constitutive mutations, such as S37E, may be a key driving factor for tumorigenesis (22–24). In a study using a mouse model of spontaneous ACP, SOX2<sup>+</sup> adult pituitary stem cells harboring a degradation-resistant form of  $\beta$ -catenin successfully induced tumorigenesis with features of ACP (25). However, nuclear accumulation of  $\beta$ -catenin was seen

<sup>1</sup>Department of Neurosurgery, West China Hospital, Sichuan University, Chengdu, 610041, China. <sup>2</sup>Institute of Clinical Pathology, West China Hospital, Sichuan University, Chengdu, 610041, China. <sup>3</sup>Department of Gastroenterology, Qilu Hospital of Shandong University, Jinan, 250000, China. <sup>4</sup>Huaxi MR Research Center (HMRR), Department of Radiology, Functional and Molecular Imaging Key Laboratory of Sichuan Province, West China Hospital, Sichuan University, Chengdu, 610041, China. <sup>5</sup>Faculty of Dentistry, The University of Hong Kong, Sai Ying Pun, 999077, Hong Kong. <sup>6</sup>Department of Thoracic Surgery/Institute of Thoracic Oncology, West China Hospital, Sichuan University, Chengdu, 610041, China. \*Corresponding author. Email: gzhang6@me.com (G.Z.); yhchen@scu.edu.cn (Y.C.); xujg@scu.edu.cn (J.X.)  
†These authors contributed equally to this work.

only in sporadic cells, while the majority of cells exhibited normal membrane localization of  $\beta$ -catenin, suggesting the potential tumor heterogeneity of ACP (26, 27). Furthermore, therapeutic strategies targeting  $\beta$ -catenin have not been efficacious, suggesting that there may be multiple underlying factors involved in the process of tumor progression (7).

Chronic inflammation and functional impairment of the central nervous system, which are closely related to patient prognosis and quality of life and survival, have accompanied most of the course of ACP development. However, the molecular mechanisms remain unclear. Reactive glial scars, which arise during ACP invasion into brain tissue, surround the tumor and endow ACP with a unique tumor microenvironment (TME) containing diverse immune cells and glial cells (28–30). Insight into the function and clinical significance of immune cells in ACP tissues has been provided by our previous study (31). In contrast to most brain tumors, the lack of restriction of the blood-brain barrier allows ACP to more frequently come into contact with infiltrating immune cells (32–34). Therefore, further comprehensive characterization of the immune landscape of ACP is needed. Furthermore, as the buffering zone for ACP to invade brain tissue, the glial scar tissue is enriched with abundant astrocytes and oligodendrocyte lineage cells (OLs), which play a potentially vital role in remodeling local tissue microenvironment that facilitates ACP progression. Considering the severe impairment of ACP in the central nervous system that is unavoidable, such as endocrine deficits (52 to 87%) and visual impairments (62 to 84%), dissecting the interaction between the tumor and the glial scar is crucial (6).

It is difficult to identify specific cell types and their cross-talk by analyzing traditional bulk transcriptomics data when the tumor is interrogated on a whole level. The latest development of single-cell RNA sequencing (scRNA-seq) technology provides us with the ability to obtain a more detailed perspective of intratumor heterogeneity and the composition of the TME at single-cell resolution (35). Therefore, we performed scRNA-seq and analyzed the transcriptomes of 27,696 single cells from three ACP tumor specimens and adjacent glial scars in this study. We further integrated scRNA-seq data of 8453 peripheral blood mononuclear cells and 7889 normal brain tissue cells from public databases to reveal the functional characteristics of nonneoplastic cells in the ACP TME. Our work innovatively describes the unique classification of neoplastic cells and the complex TME of ACP, which will not only promote our understanding of the composition and structure of ACP cells but also provide in-depth mechanistic insights into the diagnosis, treatment, and progression of ACP.

## RESULTS

### Single-cell expression atlas and cell type identification in ACP TME

We collected tumor tissues derived from three patients with ACP to perform scRNA-seq (Fig. 1A and table S1). First, our pathological examination confirmed that their tumor radiological imaging and immunostaining of anti- $\beta$ -catenin and anti-LEF1 antibodies were in line with the classic features of ACP (fig. S1, A and B). In addition, we also performed bulk RNA and exome sequencing on the aforementioned ACP tumors to gain insight into their basic properties. The transcriptional signatures and activating mutations of *CTNNB1* exhibited by these tumor tissues were consistent with

the typical genomic pattern of ACP (fig. S1, C and D, and table S2) (12, 36). Eventually, we obtained a total of 27,696 cells for scRNA-seq, and the average number of genes detected per cell was 2701 (fig. S1, E to I). Following rigorous quality control, we performed the clustering analysis by using an unsupervised method and obtained 18 cell subpopulations (fig. S2, A and B). According to the transcriptomic characteristics of the subpopulations, 27,696 single cells were further grouped into eight main clusters (Fig. 1B). Cluster-specific marker genes were used to annotate the classic cell types based on previous studies, including *CDH1* and *EPCAM* for epithelial cells, *LYZ* and *CD68* for myeloid cells, *CD3E* for T cells, *CD79A* for B cells, *AQP4* and *GFAP* for astrocytes, *OLIG2* and *SOX10* for oligodendrocyte precursor progenitor cells (OPCs), *MOG* for oligodendrocytes, and *PECAM1* for endothelial cells (Fig. 1, B and C, and fig. S2B) (12, 25). It is worth noting that the rare endothelial cells may reflect biases in tissue dissociation and microfluidic-based cell capture. Compared with other samples, the ACP-2, which was obtained from the junction of tumor and glial scar, contained more immune cells and glial cell components. Multiplex immunohistochemistry (IHC) staining identified the distribution of the main cell types, including *CDH1* for epithelial cells, *CD3* for T cells, *CD68* for myeloid cells, *GFAP* for astrocytes, *OLIG2* for the OLs, and the tumor-specific mutated gene *CTNNB1* in the TME (Fig. 1D). Furthermore, we identified neoplastic cells by two complementary approaches. First, previous studies have proposed that ACP is a type of tumor composed of squamous epithelial cells (37). Multi-IHC staining indicated that the epithelial cells located in CDH1-positive staining area conformed to the classic ACP pathological characteristics, permitting us to spatially locate and further resolve neoplastic cells in ACP (Fig. 1D and fig. S2C). Second, by performing inferCNV analysis, we found higher levels of copy number variation (CNV) for epithelial cells as compared with immune cells and glial cells (Fig. 1E). As a result, 23,535 cells were defined as neoplastic cells. To verify the accuracy of the identification of neoplastic cells, we curated gene signatures of ACP from previous studies based on the bulk transcriptome data and examined their expression levels in various subpopulations (19, 38). Subsequently, we showed substantially higher expression levels of canonical ACP marker genes in all the neoplastic cell clusters, although we noted a biased distribution (fig. S2D). Immunostaining results showed that most immune cells and glial cells in the TME of ACP were located outside of tumor structure, which were composed mainly of reactive glial scar tissue (fig. S2E).

### Characterization of transcriptional heterogeneity of neoplastic cells in ACP

The initial aggregation of neoplastic cells revealed patient-specific clusters (fig. S3A). Tumors derived from individual patients showed preferential expression of more than 150 genes, manifested by different levels of enrichment of classic tumor pathways and metabolic pathways (fig. S3, B to D). To characterize the intratumor heterogeneity of neoplastic cells, we analyzed clusters of coexpressed genes in each tumor based on nonnegative matrix factorization (NMF) and obtained a total of 25 intratumor signatures (table S3). Taking ACP-3 as an example, the NMF results demonstrated complex intratumoral expression features in ACP (Fig. 2A). By assuming that some intratumoral signatures could reflect common features of ACP, we subsequently identified four prominent meta-signatures across tumors by performing correlation cluster analysis

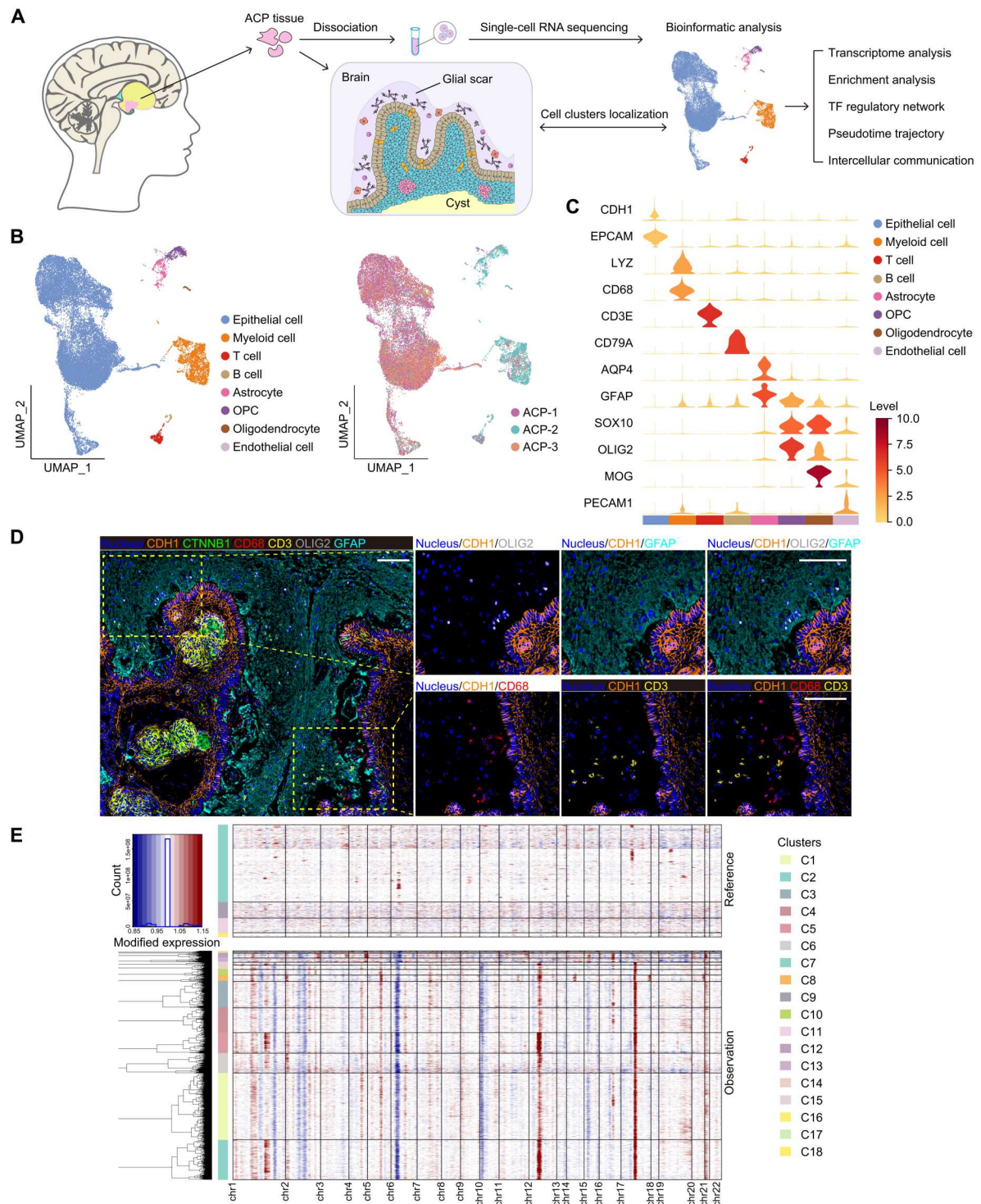


**Fig. 1. Single-cell transcriptomic analysis identifies cell types in ACP.** (A) Workflow demonstrates the process of sample collection, single-cell suspension preparation, single-cell sequencing, and bioinformatics-based analysis to reveal tumor heterogeneity. (B) UMAP plots of 27,696 cells showing the major cell types and sample origins in ACP tissues based on analysis of 10X GENOMICS scRNA-seq data. (C) Violin plots show the expression levels of specific marker genes for eight major cell types. (D) Multi-IHC staining with anti-CDH1 (epithelial cells), anti-CTNNB1 (ACP classic mutant gene), anti-CD68 (macrophages), anti-CD3 (T cells), anti-OLIG2 (oligodendrocyte lineages), and anti-GFAP (astrocytes) antibodies to localize the histological distribution of major cell types in ACP. Scale bars, 50  $\mu$ m. (E) Heatmap showing the chromosomal map of single-cell large-scale CNVs inferred by scRNA-seq. Use immune cells as a reference, and amplifications (red) or deletions (blue) were inferred by averaging expression over 100-gene stretches on every chromosome.

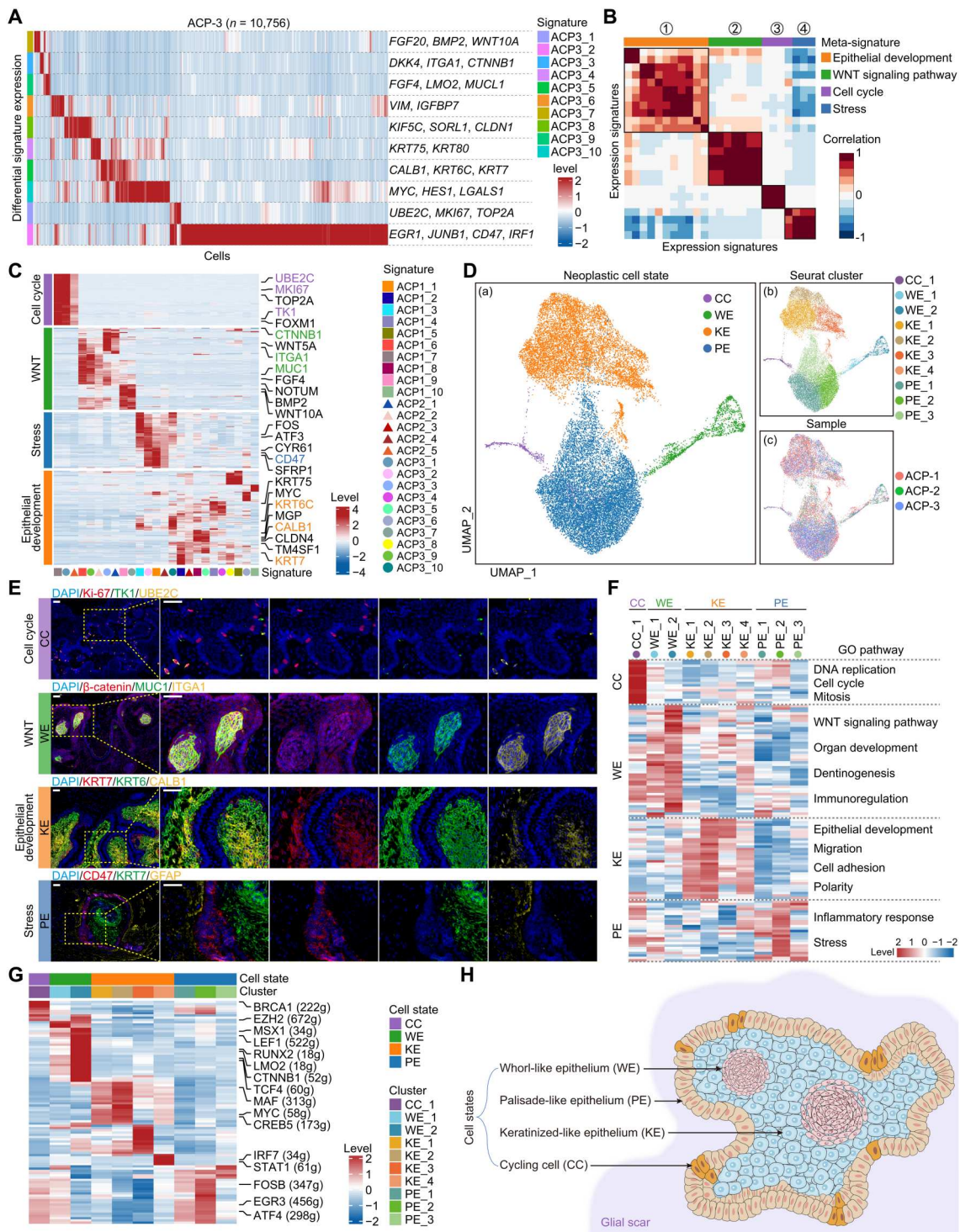


**Fig. 2. Deciphering expression programs revealed distinct clusters of neoplastic cells in ACP.** (A) Heatmap showing gene expression signatures parsed from a representative tumor (ACP-3) using NMF. Each expression signature was numbered, and its corresponding genes were displayed (right). (B) Pearson correlation clustering of 25 intratumoral expression signatures. Four regions consisting of clusters of highly correlated signatures were identified as meta-signatures. (C) Heatmap showing the expression levels of meta-signatures marker genes in each intratumoral signature. (D) UMAP plots showing the distribution of cell states (a), clusters (b), and sample origins (c) in ACP neoplastic cells. Ten neoplastic clusters (b) were generated by Seurat analysis and summarized into four cell states (a) based on the AddModuleScore scores. (E) Multi-IHC showing the histopathological distribution of CC (anti-Ki-67, TK1, and UBE2C), WE (anti- $\beta$ -catenin, MUC1, and ITGA1), KE (anti-KRT7, KRT6, and CALB1), and PE (anti-CD47, KRT7, and GFAP). Scale bars, 50  $\mu$ m. (F) Heatmap showing differences in gene ontology (GO) pathway activity between neoplastic clusters of ACP scored by GSVA. (G) Heatmap showing differences in TF activity across neoplastic clusters of ACP scored by SCENIC. (H) Cartoon model showing the spatial distribution of major neoplastic cell states in ACP tissue.

of 25 signatures (Fig. 2B). These four meta-signatures contained their own unique gene sets (Fig. 2C and table S4). The first meta-signature was related to epithelial development and was composed mainly of keratin genes, such as *KRT6C* and *KRT7*, as well as cell adhesion molecules, such as *LGALS3* and *CLDN4*. The second meta-signature was composed of WNT signaling pathway molecules, such as *LEF1* and *WNT5A*, and downstream target genes, such as *FGF4* and *BMP4*. Most of genes in the third meta-signature were related to cell cycle, which was composed of mitotic genes, DNA replication-, and transcription-related genes such as *UBE2C*, *CENPK*, and *TOP2A*. Genes in the fourth meta-signature were related to stress responses and cellular activation, such as *FOS*, *JUN*, and *EGR2* (Fig. 2C). Next, we regrouped all 23,535 neoplastic cells into 10 clusters through Seurat integrated clustering (fig. S4A). Subsequently, on the basis of the abovementioned marker gene sets of meta-signatures, we calculated functional scores for all neoplastic cells, which permitted us to lastly define four major cell states (Fig. 2D and fig. S4B). According to previous studies, ACP has unique histopathological structures, such as palisading epithelium, whorl-like structures, and stellate reticulum (19). We hypothesized that neoplastic cells with similar transcriptional characteristics and functions tended to be spatially located in neighboring areas. Immunostaining of specific markers revealed histologically unique locations of different cell states (Fig. 2E). According to the histological distributions and molecular functions of the neoplastic cells, we defined the four cell states with specific meta-signatures as: (i) keratinized-like epithelium (KE) with epithelial development feature, (ii) whorl-like epithelium (WE) with WNT feature, (iii) cycling cell (CC) with cell cycle feature, and (iv) palisade-like epithelium (PE) with stress feature. PE was distributed mainly along the outermost side of the tumor tissue, arranged closely in a fence-like manner, and was in contact with the outer stromal tissue. WE was distributed mainly in epithelial whorl-like structures, showing the expression pattern of nuclear accumulation of  $\beta$ -catenin. KE expressing a unique spectrum of cytokeratins was mainly distributed along the tumor inner side in which the stellate reticulum was located. CC was scattered mainly in the PE but rarely in other structures. In stark contrast, neoplastic cells clustered distribute in ACP, multiple types of cells grow intertwined each other in other kinds of tumors. Furthermore, we validated this distribution pattern in additional 18 ACP tumor specimens by IHC staining (fig. S5). These cellular states appeared to reflect essential features of ACP during tumor development. Although ACP-2 contained only a few neoplastic cells, the proportions of the four cell states were still similar to those of other samples. We also found that epithelial whorl-like structures, which were previously implicated in mutation-induced persistent activation of the WNT pathway, were composed of two cell states, WE and KE. Only WE shown nuclear accumulation of  $\beta$ -catenin (fig. S4C).

To illustrate the functional heterogeneity of neoplastic cells, we carried out clustering analysis via gene set variation analysis (GSVA) to infer the biological functions of neoplastic clusters (Fig. 2F and fig. S4D). GSVA revealed that the WE was related to activation of the WNT signaling pathway, organ development, and dentinogenesis. Pathways such as epithelial development, cell adhesion, cell movement and migration, and cell polarity regulation were up-regulated in KE. Endoplasmic reticulum stress and inflammation were enriched in PE, which may be due to stronger inflammatory stimulation presented in the TME of ACP.

Furthermore, we sought to correlate transcriptome differences with transcription factor (TF) motifs across all neoplastic clusters by inferring a single-cell regulatory network and conducting clustering (SCENIC) analysis. SCENIC analysis identified a set of TFs associated with biological signatures of distinct neoplastic clusters in ACP. The results showed that cell clusters within the same cell states exhibited similar patterns of TF regulation (Fig. 2G). In addition, we found that the key transcription motifs of *LEF1*, *TCF4*, and *CTNNB1* in the WNT signaling pathway were activated in WE\_1 and WE\_2 (fig. S4E). Previous studies demonstrated that the constitutive activating mutation of *CTNNB1* is responsible for activating the WNT pathway in ACP, and this mutation covers almost all neoplastic cells (22). In this study, WNT-related transcriptional motifs were substantially activated in WE relative to other cell states. Immunostaining confirmed that the  $\beta$ -catenin and *LEF1* were specifically expressed in WE and showed nuclear accumulation (fig. S1B). In addition, we found that the osteogenesis- and dentinogenesis-related TFs *RUNX2* and *MSX1* were substantially activated in WE (Fig. 2G). Motifs of *MYC* and *MAF* were activated in the KE (Fig. 2G), thereby regulating downstream cell adhesion molecules such as *CLDN3* and *CLDN4* as well as the malignant tumor progression-related gene *MGP* (39, 40). In short, we identified four distinct neoplastic cell states with characteristic transcriptional regulatory networks and regular histological distribution, which provided further insight into the intratumoral heterogeneity of ACP (Fig. 2H).

### Pseudotime trajectory analysis of neoplastic cells in ACP

Although the WE and KE revealed notable transcriptomic characteristics, their proliferative activities were low (Fig. 2E and fig. S4C). In addition, there were some transcriptional features and TF motifs shared by clusters belonging to different cell states, suggesting that transformation of cell states might occur among clusters. To test this hypothesis, we further performed RNA velocity analysis to explore the transcriptional dynamics exhibited by subsets of neoplastic cells. Transcriptional rate analysis suggested that ACP neoplastic cells might start from PE and follow two different evolutionary directions. One of which evolved toward the WE cell states that was highly activated by the WNT signaling pathway. Whereas the other evolved toward the direction of KE, in which epithelial differentiation was more pronounced (Fig. 3A). Immunostaining of KE and WE showed mutually exclusive histological distribution, supporting that they belonged to cell groups with different evolutionary paths (fig. S4C). Differentiation marker, including *LEF1*, *TCF4*, and *WNT5A* for WE and *KRT6C*, *KRT7*, and *KRT75* for KE, also showed a high transcriptional activity in the evolutionary paths (Fig. 3B). Notably, whorl-like neoplastic cells with nuclear accumulation of  $\beta$ -catenin have been implicated as drivers of ACP tumorigenesis in previous studies (6, 38). Experimentally, up-regulated  $\beta$ -catenin in nuclear has induced spontaneous tumor formation similar to human ACP in transgenic mice (41, 42). Unlike classical tumor germinal centers, whorl-like structures exhibit biological features of senescence, including cell cycle arrest and senescence-associated secretory phenotype (25, 42). In addition, inferCNV analysis revealed a remarkably complex pattern of CNVs in WE (fig. S6A). According to previous classifications of known cellular states, CNV patterns were associated with a remarkable heterogeneity and functional states of neoplastic cells (43, 44). We reconstructed patient-specific CNV patterns based on principal components analysis

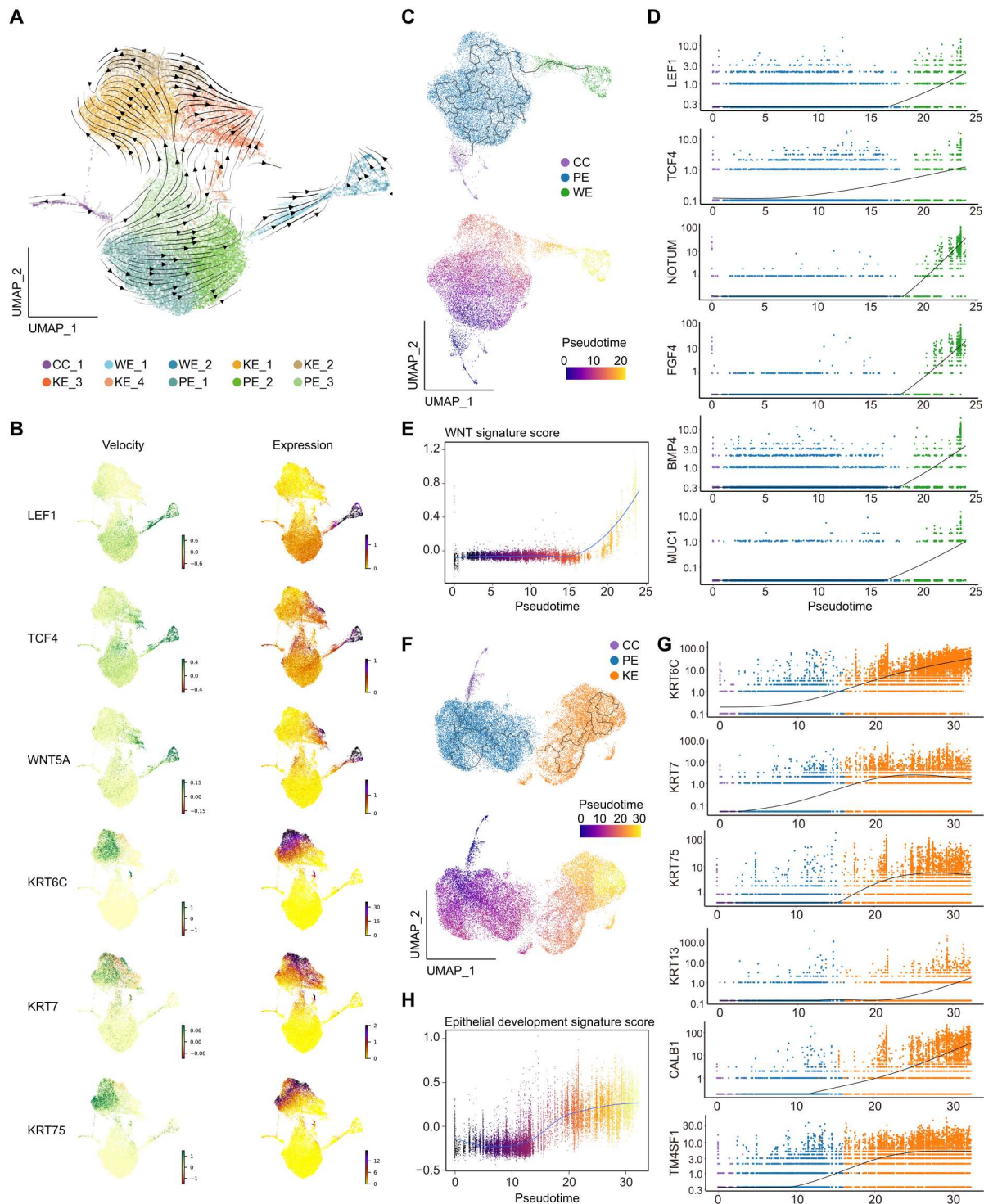


**Fig. 3. The evolutionary trajectory of neoplastic cells in ACP.** (A) Inferred evolutionary trajectories of all ACP neoplastic cells by RNA velocity. (B) UMAP plots showing RNA velocity and expression levels of WE (*LEF1*, *TCF4*, and *WNT5A*) and KE (*KRT6C*, *KRT7*, and *KRT75*) marker genes. (C) Pseudotime evolution trajectories inferred by Monocle3 after reclustering of neoplastic cell states PE, WE, and CC. (D) Traceplots of WE marker genes expression levels along pseudotime. (E) Traceplots of the WNT signature score along pseudotime. (F) Pseudotime evolution trajectories inferred by Monocle3 after reclustering of neoplastic cell states PE, KE, and CC. (G) Traceplots of KE marker genes expression levels along pseudotime. (H) Traceplots of the epithelial development signature score along pseudotime.

(PCA) dimensionality reduction and cluster analysis, which revealed a unique distribution of WE (fig. S6B). Next, the clonality tree was generated using the UPhyloplot2 algorithm (45, 46). A specific set of CNV accumulations related to WE was observed, such as gain of chr11q, chr14q, and chr20p, which may be potentially linked to an increase in the genomic instability of the aging state (fig. S6C). To further delineate gene expression patterns depicting the evolution of neoplastic cells, we performed Monocle3 analysis of two evolutionary paths separately (Fig. 3, C and F). WNT-related genes showed a trend of positive regulation along the pseudotime axis of PE-WE evolution (Fig. 3, D and E). Similarly, epithelial differentiation marker genes such as *KRT6C*, *KRT7*, *KRT75*, *KRT13*, and cell adhesion-related markers *TM4SF1* showed a positive regulatory trend in the PE-KE evolution axis with pseudotime (Fig. 3, G and H). In summary, our results revealed potential evolutionary trajectories among neoplastic cell clusters in ACP.

### T cell clustering and subtype analysis in ACP

After integrating immune cells with published scRNA-seq data of peripheral blood mononuclear cells (PBMCs) derived from one healthy volunteer, we regrouped the cells to obtain an atlas of immune cells containing more than 11,000 cells (Fig. 4A and fig. S7, A and B). Regrouping T cells identified a total of 10 clusters, of which three clusters were derived mainly from tumor tissues (Fig. 4B and fig. S7, C to E). We further interrogated the expression of typical T cell markers in 10 clusters and scored immune function based on the gene expression of classic markers (Fig. 4C and fig. S7F). The analysis further revealed that the CD4-C4-FOXP3 and CD4-C5-CTLA4 clusters represented CD25<sup>+</sup>/FOXP3<sup>+</sup> regulatory T cells (T<sub>regs</sub>). CD4-C4-FOXP3 originated mainly from peripheral blood, while CD4-C5-CTLA4 originated mainly from tumor tissues. The CD4-C5-CTLA4 cluster had the highest scores of T<sub>reg</sub> and immune cells exhaustion, indicative of its immunosuppressive state. The CD4-C3-CD69 cluster from tumors had a strong immune exhaustion score but did not express any T<sub>reg</sub> markers, which may represent a population of exhausted CD4<sup>+</sup> T cells in the TME. The CD8-C3-GZMK, CD8-C4-CX3CR1, and CD8-C5-IFNG clusters showed higher expression levels of cytotoxicity markers, such as *GZMK*, *NKG7*, and *GZMH*. However, the CD8-C5-IFNG cluster did not have the highest cytotoxicity score but instead had the most substantial exhaustion score.

Immune checkpoint blockade (ICB) has been proposed as a promising treatment for ACP, but its efficacy is interfered by the complex immunosuppressive TME in ACP (47, 48). Previous studies in our laboratory and others have suggested complex expression patterns of B7 family ligands/receptors in craniopharyngiomas (7, 31, 49, 50). To further elucidate the functional characteristics of tumor-infiltrating T cells, we performed differential expression analysis of T<sub>reg</sub> and cytotoxic T cells derived from neoplastic and nonneoplastic tissues (Fig. 4D). For the two T<sub>reg</sub> clusters, CD4-C5-CTLA4 exhibited higher expression of chemokine receptors (such as *CXCR6*) and tissue-resident signatures (such as *CD69* and *ITGAE*), which may represent a common feature of tumor-infiltrating T<sub>regs</sub>. Furthermore, our analysis confirmed that tumor-derived T<sub>regs</sub> expressed stronger immune checkpoints, such as *CTLA4*, *TIGIT*, *TNFRSF4*, *TNFRSF9*, *HAVCR2*, *LAYN*, and *PDCD1*. These molecules are widely involved in tumor immunosuppression, suggesting a shift in the functional status of ACP-infiltrating T<sub>regs</sub> toward immunosuppression. We used a gene set of

tumor-induced antigen-experienced T<sub>reg</sub> markers to assess the immune function status of T<sub>regs</sub> (table S5) (51). ACP-derived T<sub>regs</sub> had substantially higher scores, which further supports that their activation led to functional tumor T<sub>regs</sub> (fig. S7G). The GSVA results suggested that ACP-derived T<sub>regs</sub> showed notable differences in multiple biological pathways associated with tumor progression, such as “blood vessel morphogenesis” and “transforming growth factor beta1 production” (fig. S7H). Meanwhile, the activation of macrophage chemotaxis and stress-related pathways reflected the response and regulation of ACP-derived T<sub>regs</sub> in the tumor inflammatory microenvironment. In addition, tumor-derived cytotoxic T cells expressed *IFNG* and the chemokines *CCL3*, *CCL4*, and *CCL5*, suggesting that they might be activated (Fig. 4E). In short, our study revealed the immunosuppressive status of tumor-infiltrating T cells in the ACP TME and their potential role in coordinating ACP progression.

### Heterogeneity and state analysis of myeloid subpopulations in ACP

We reclustered 4205 myeloid cells consisting of 2291 tumor-derived cells and 1914 nonneoplastic tissue-derived cells. Myeloid cells showed a notable degree of heterogeneity and were divided into 10 clusters, including monocytes/macrophages, dendritic cells, and neutrophils, based on the expression of known classic markers (Fig. 4, F and G, and fig. S8, A and B). Most macrophages originated from tumor tissues, suggesting the influence of the ACP TME on the differentiation of macrophages. Accumulating evidence suggested that chronic inflammatory processes play a key role in ACP tumorigenesis and development, while the genesis of cystic components was closely associated with poor prognosis (47, 52). To further define the characteristics of tumor-infiltrating monocytes/macrophages, we scored all monocytes/macrophages according to the classic characteristic genes of M1/M2 (table S6). We found that the tumor-derived monocyte/macrophage subpopulations had higher M1 and M2 scores (Fig. 4H). There was a significant positive correlation of feature scores of M1 and M2 between all monocytes/macrophages ( $R = 0.67$ ,  $P < 0.0001$ ) (Fig. 4I), indicating that activation of macrophages in the ACP TME may adopt the M1-M2 coupling activation mode. The results of differential gene expression analysis showed that tumor-derived monocytes/macrophages highly expressed polarization markers (such as *CD163*) and secreted abundant chemokines (such as *CXCL8*, *CXCL16*, *CCL2*, *CCL3*, and *CCL4*), which may partially explain the recruitment of tumor-infiltrating immune cells and the secretion of inflammatory cyst fluid in ACP (fig. S8C). The clustering analysis via GSVA suggested that the inflammatory response, inflammatory factor release, cell chemotaxis, and macrophage differentiation were substantially up-regulated in the tumor-infiltrating monocytes/macrophages (fig. S8D). SCENIC analysis identified a set of regulation patterns of tumor-specific TFs in monocytes/macrophages, such as *MAF*, *NFIL3*, *CEBPD*, *CREM*, etc. (Fig. 4J and fig. S8E). Previous studies have shown that *MAF* and *CEBPD* are essential for the regulation of macrophage differentiation and inflammatory signaling (53, 54). The results of the SCENIC analysis suggest that ACP-derived macrophages undergo functional activation and are involved in the regulation of local inflammatory responses in the TME, which may contribute to the up-regulation of pro-inflammatory mediator levels at the hypothalamus and pituitary during ACP invasion.

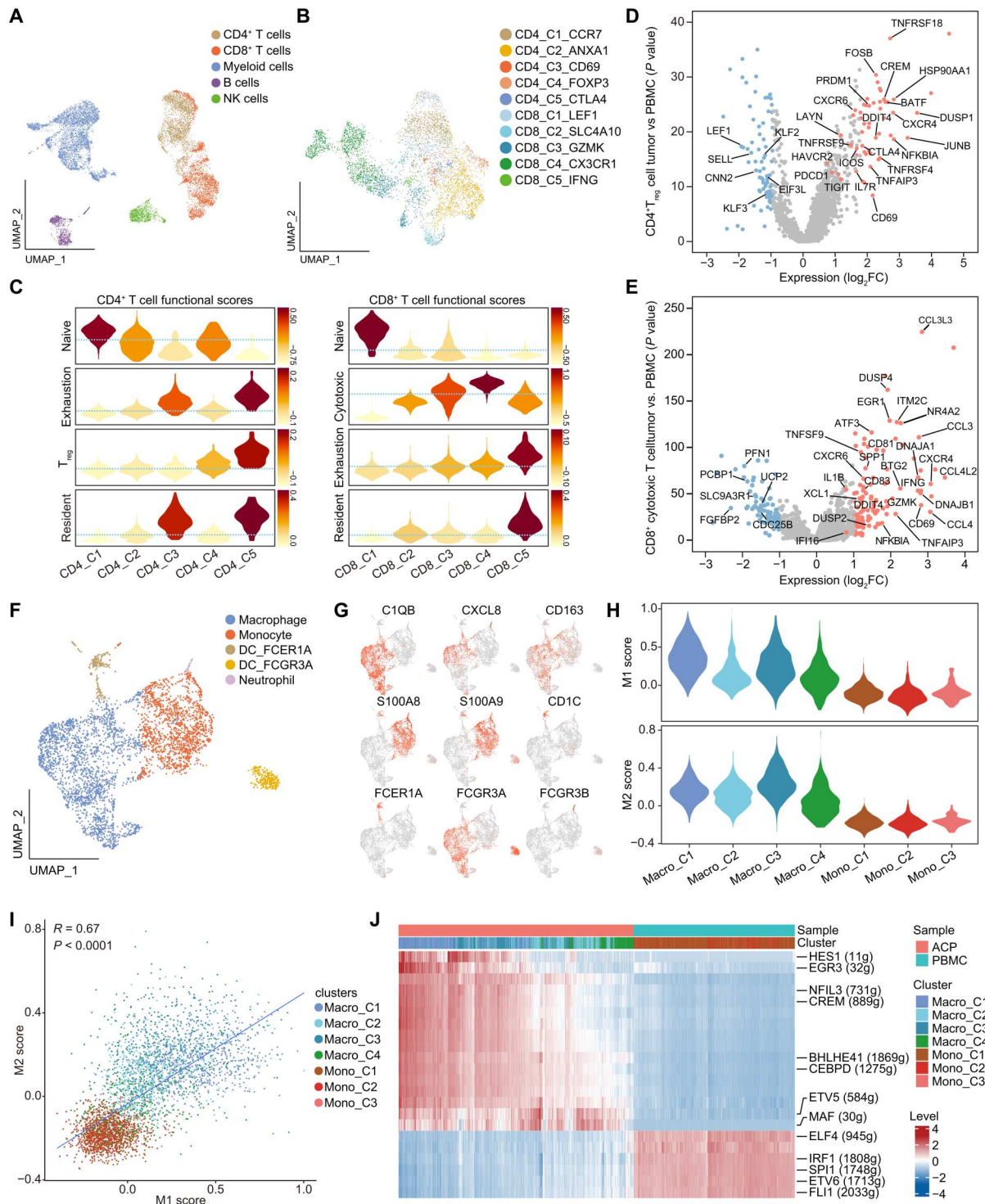


**Fig. 4. Assessing the functional states of tumor-infiltrating immune cells in ACP.** (A) UMAP plot showing the reclustering of all immune cells in ACPs and PBMCs after the integration of public data. CD4<sup>+</sup> T cells, CD8<sup>+</sup> T cells, myeloid cells, B cells, and natural killer (NK) cells were identified as the main cell types. (B) UMAP plot showing 10 clusters identified in T cell reclustering. (C) Violin plots showing naïve, exhaustive, cytotoxic, T<sub>reg</sub>, and resident characteristics in CD4<sup>+</sup> T cells and CD8<sup>+</sup> T cells scored by AddModuleScore function. Dependent gene sets refer to table S5. (D) Volcano plot showing differentially expressed genes between neoplastic and nonneoplastic tissue-derived T<sub>reg</sub>s. (E) Volcano plot showing differential genes of neoplastic and nonneoplastic tissue-derived cytotoxic T cells. (F) UMAP plot showing the reclustering of myeloid cells. (G) UMAP plots showing the expression and distribution of canonical myeloid marker genes in myeloid cells. (H) Violin plots showing representative M1 and M2 characteristics in monocytes/macrophages scored by AddModuleScore function. Dependent gene sets refer to table S6. (I) Dot plot showing the correlation between the M1 and M2 scores. (J) Heatmap showing differences in TF activity in monocytes/macrophages (column). FC, fold change.

## Deciphering the molecular phenotype and functional characteristics of glial cells in the glial scar

The process of ACP invading brain tissue induces gliosis outside the tumor and the formation of glial scar, which represents a unique TME for ACP (10, 19). To identify the cellular heterogeneity and transcriptomic characteristics of glial scars, we extracted tumor-derived glial cells and integrated scRNA-seq data derived from eight cases of brain tissues for reclustering, which led to a transcriptome of 5802 glial cells. On the basis of the differential gene expression levels of each cluster and classical markers, we identified five cell types, including astrocytes, oligodendrocytes, OPCs, neural progenitor cells, and neurons (Fig. 5A and fig. S9, A and B). We found that tumor tissue–derived astrocytes expressed higher levels of glial fibrillary acidic protein (GFAP), one of the major intermediate filament proteins of mature astrocytes, relative to brain tissue–derived astrocytes. The antennae of astrocytes derived from tumor tissue were thicker, and the GFAP<sup>+</sup> glial fibers of adjacent astrocytes overlapped, crossed, and entangled each other to form glial scars (fig. S9, C and D). Previous studies have suggested that this phenomenon is characteristic of activated astrocytes (55, 56). Compared with nonneoplastic tissues, tumor-derived astrocytes showed a notable enrichment of pathways such as the inflammatory response, interferon- $\gamma$  (IFN- $\gamma$ ) response, and astrocyte activation (fig. S9E). In addition, the abnormal activation of multiple metabolic pathways was observed in tumor-derived astrocytes, such as arachidonic acid metabolism and mucin-type O-glycan biosynthesis fatty acid biosynthesis, suggesting a metabolic adaptation of the TME regulated by ACP tumors (fig. S9F).

OLs are widely distributed along the outer side of tumor tissue and are involved in forming glial scars and remodeling the TME. To further explore its functional characteristics, we applied NMF to all oligodendrocytes and OPCs, which resulted in 10 expression signatures (fig. S10A and table S7). Among these signatures, OL-3 and OL-4 were specifically enriched in tumor tissue–derived OLs, which were composed mainly of genes related to oligodendrocyte development and central nervous system myelination, such as *MAG*, *MOBP*, and *FGFR2* (fig. S10A), suggesting that tumor-derived OLs may be involved in neural repair during tumor invasion of brain tissue. Unexpectedly, we found that OL-9, a tumor-specific signature, is composed of immunoregulatory genes, suggesting that there may be a distinct immunophenotypic oligodendrocyte lineage in the ACP TME. Antigen presentation–related genes including major histocompatibility complex II (MHC-II)–encoding genes (such as *HLA-DRA*, *HLA-DRB1*, and *CD74*) and immune-type proteasome constituent molecules (such as *PSMB8* and *PSMB9*) were enriched in OL-9. Previous studies have reported this immunophenotypic OLs (iOLs) in models of central system autoimmune diseases such as multiple sclerosis (MS) and experimental autoimmune encephalomyelitis (EAE) (57–60). Subsequently, we examined the gene expression levels of OLs in each cluster according to the classical features described in previous studies (Fig. 5B). Compared to nonneoplastic tissue, neoplastic tissue–derived OLs had higher expression levels of MHC-I and MHC-II constituent molecules, including *B2M*, *HLA-A*, *HLA-B*, *HLA-C*, *HLA-DRA*, and *HLA-DRB1*, and genes related to antigen processing and presentation, including *PSMB8*, *PSMB9*, *TAPBP*, and *TAP1*, which suggested that they conformed to the classical features of immune-characterized OLs described in previous studies. Subsequently, we localized OLs with immunological properties in the

TME by performing multi-IHC staining of MHC-II molecules (HLA-DR and CD74) and the OLs marker OLIG2 (Fig. 5C). CD68 was used as a negative marker to exclude myeloid cells. Furthermore, we compared the expression profiles between neoplastic and nonneoplastic tissue derived OPCs (Fig. 5, D and E). The integrated analyses of differentially expressed genes and pathway enrichment revealed functional characteristics of tumor-derived OPCs. Except for MHC-II molecules and antigen-presenting genes, tumor-derived OPCs substantially expressed genes related to the IFN response (*IFITM3* and *IFI16*), endoplasmic reticulum stress (*DNAJB1* and *HSPA1B*), and DNA damage (*CDKN2A* and *BTG2*). Previous reports have suggested that the abnormal immune inflammatory response may be an inducing condition that promotes the functional phenotypic transformation of OLs and the expression of MHC-II molecules, especially the stimulation of IFN- $\gamma$  (58). The results of enzyme-linked immunosorbent assay (ELISA) and Western blot experiments indicated that ACP had a higher expression level of IFN- $\gamma$  relative to brain tissue (fig. S10, B and C). In addition, the results of multi-IHC staining showed higher IFN- $\gamma$  expression level in the ACP TME where OLs were located relative to the brain tissue environment (fig. S10D). We found that CD8<sup>+</sup> T cells were also distributed in a close proximity to OLs, which was not observed in brain tissue (fig. S10D). Previous studies have suggested that CD8<sup>+</sup> T cells are capable of recognizing iOLs and exerting cytotoxic effects through antigen presentation, which may contribute to neural damage upon ACP tumor progression (59). Subsequently, SCENIC analysis revealed a potential regulatory network of TFs across subtypes in the OLs (Fig. 5F). For example, *IRF1* and *STAT3* were identified as candidate TFs underlying the gene expression differences in iOLs. *IRF1* and *STAT3* are reported to be up-regulated after stimulation by immune and inflammatory factors (especially IFN- $\gamma$ ) and are involved in various downstream pathways, such as oxidative stress and apoptosis, as response regulators. To determine whether iOLs are also present in other brain tumors, we analyzed the glioblastoma (GBM) scRNA-seq data from public dataset (61). After clustering and cell annotation, we calculated the immune score of each cluster based on the gene set of antigen presentation process (including *HLA-DRA*, *HLA-DRB1*, *HLA-DRB5*, *HLA-DPA1*, *HLA-DPB1*, *CD74*, *PSMB8*, *PSMB9*, *TAP1*, and *TAPBP*; fig. S11, A to C). However, we did not observe OL clusters with similar transcriptional characteristics to iOLs in GBM (fig. S11C). As an immunologically cold tumor, the immune microenvironment of GBM may not support the induction and transformation of iOLs.

Then, we focused on transcriptomic differences in iOLs between tumor and autoimmune disease models. Differential gene expression analysis revealed that cell adhesion–related extracellular matrix components, such as proteoglycans (including *VCAN*, *CSPG4*, *SDC3*, *LGALS1*, and *LGALS3*) and *VIM*, were up-regulated in tumor-derived iOLs (fig. S10E). We found that OLs with high expression levels of *VCAN* were widely distributed outside the tumor tissue by immunostaining (fig. S10F). Previous studies support that *VCAN* is one of the key components of the extracellular matrix in various malignant tumors and contributes to tumor development and the formation of the preinvasive microenvironment, suggesting that OLs may be involved in ACP TME remodeling as potential regulators (62, 63). We subsequently analyzed RNA sequencing data derived from MS samples in public datasets and did not find similar signatures, suggesting that the influence of the TME

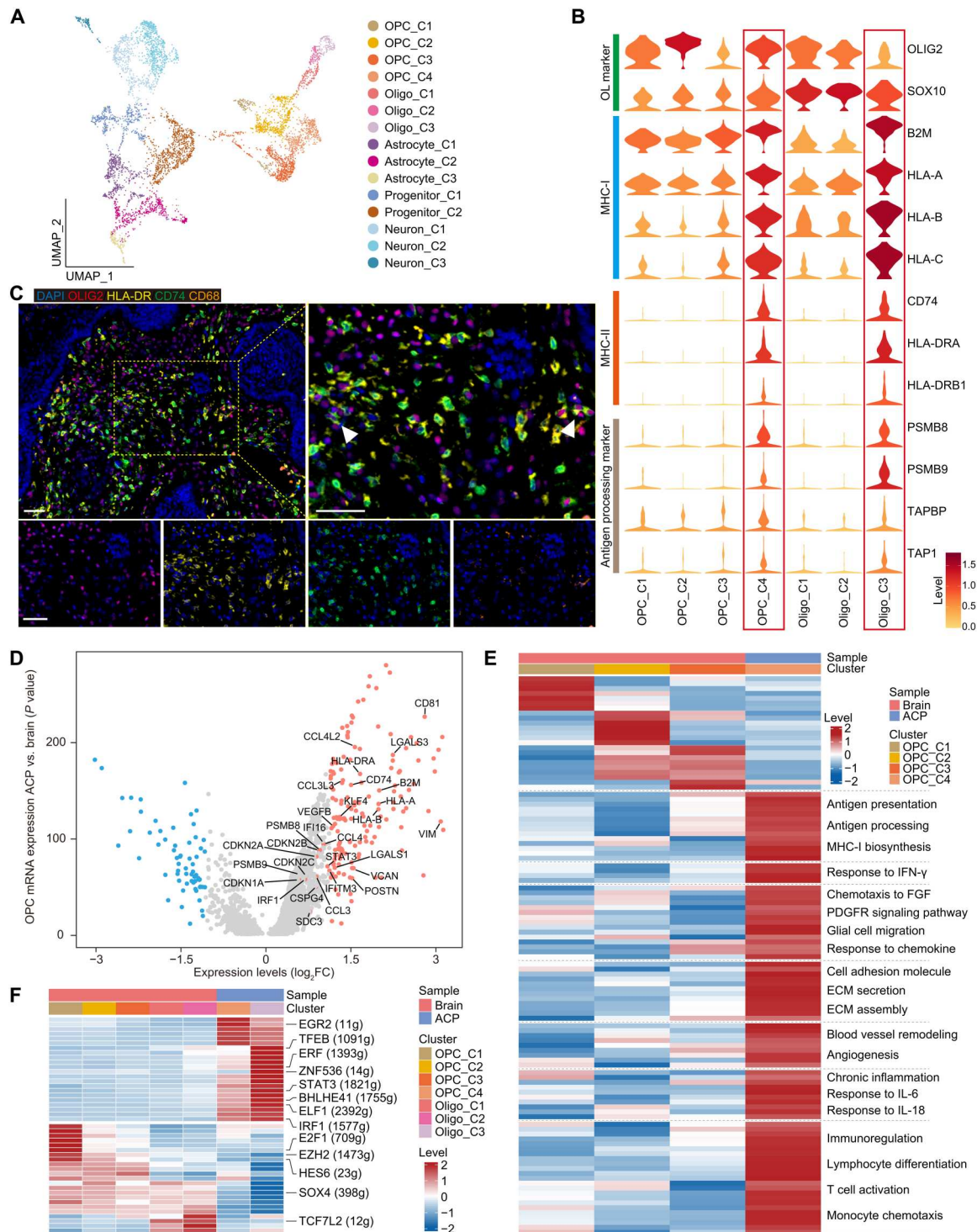


**Fig. 5. Detailed characterization of oligodendrocyte lineage in ACP.** (A) UMAP plot showing the distribution of glial cell clusters after reclustering. (B) Violin plots showing the expression levels of functional markers in oligodendrocyte lineages across different clusters. (C) Multi-IHC staining demonstrates the histological distribution of oligodendrocytes with immunological features. Arrowheads indicate iOLs. Scale bars, 50  $\mu$ m. (D) Differential gene expression profiles of tumor- and brain-derived OPCs. Genes related to antigen presentation were highly expressed in tumor-derived OPCs (red). Representative genes are labeled. (E) Heatmap showing the activation levels of differential pathways for GO enrichment analysis in OPCs across different clusters. (F) Heatmap showing differential TF activity across different clusters in the oligodendrocyte lineage revealed by SCENIC.

may induce the transformation of iOLs into a distinct tumor-promoting phenotype (fig. S10, E and F).

### Establish an intercellular communication network in the ACP TME

Next, we performed CellChat analysis to identify cell-cell interactions in the ACP TME. Potential ligand-receptor pair interactions between major cell types in the TME revealed a complex cellular communication network (fig. S12A). First, we focused on communication events that occurred within the tumor. WE\_2 mediated the most efferent and afferent events from other subpopulations in the ACP, possibly representing a signaling center and secretory hub within the tumor (Fig. 6A and fig. S12B). Considering that ACP is a WNT signaling-driven tumor, we focused on the distribution of WNT-related communication events across subpopulations. Our results indicated that WE mediated the most frequent WNT-related signaling among the four major neoplastic cell states, and the target cells receiving WNT signaling in the ACP TME consisted mainly of KE\_3, WE\_2, KE\_1, and KE\_2 (Fig. 6B). Among all neoplastic cell states, WE expressed the highest levels of WNT pathway ligands, including *WNT5A*, *WNT6*, *WNT10A*, and *WNT10B*, as well as ligand genes for its downstream related pathways, such as fibroblast growth factor (FGF) (*FGF4* and *FGF20*), bone morphogenetic protein (BMP) (*BMP4* and *BMP7*), and Hedgehog (*SHH*) signaling pathways (Fig. 6C). Their receptor distribution covered almost all neoplastic cells, suggesting that WE plays a crucial role in abnormal activation of WNT signaling and tumor development (Fig. 6C). In addition, there were some typical ECM-receptor interactions between neoplastic cells, such as *LAMB1-CD44*, *POSTN-ITGAV*, and *COL6A1-ITGB1*, which might contribute to tumor proliferation and invasion during ACP progression.

We next focused on the interaction between neoplastic cells and stromal cells in the TME (fig. S12C). Neoplastic cells secreted multiple cytokines, including *FGF2*, *FGF9*, and *PDGFA*, the receptors of which were prominently expressed in the oligodendrocyte lineages. Previous studies have demonstrated that in models of brain injury or inflammation, abundantly secreted cytokines such as *FGF2* and *PDGFA* recruit OLs to migrate to lesion sites to participate in neural repair (64–66). Furthermore, we observed that neurotrophic factors such as *BDNF*, *NTF4*, *IGF1*, and *NRG2* were enriched in the TME of ACP. Their target receptors, such as *IGF1R*, *ERBB3*, *ERBB4*, *NTRK2*, and *LIFR*, were distributed in the oligodendrocyte lineage, which may contribute to the survival and proliferation of OL cells in an inflammatory environment.

Infiltration of immune cells is a typical feature of ACP (67). Abundant expression of immunochemokines (*CXCL1*, *CXCL2*, *CXCL6*, *CXCL8*, *CXCL16*, *CCL3*, and *CCL4*) was noted in the ACP TME, while the corresponding receptors were widely expressed in T cells and macrophages (fig. S12C). This chemokine-mediated cellular communication may play critical roles in maintaining inflammatory cell infiltration and immune microenvironment homeostasis in ACP. Furthermore, we speculated that some ligand-receptor pairs (such as *MIF-CD74/CD44*, *TGFB1-TGFBRI*, *IL10-IL10RA/IL10RB*, *ADGRE5-CD55*, and *PROS1-AXL/MERTK*) in the ACP TME may be involved in the transition of the monocyte/macrophage functional state to anti-inflammatory activation, and these secretory signals were secreted mainly by neoplastic cells (fig. S12C). In previous studies, secretory signals were involved in the recruitment and chemotaxis of tumor-associated

macrophages as pleiotropic immune regulators. In addition, migration inhibition factor, transforming growth factor- $\beta$ 1 (TGF- $\beta$ 1), and interleukin-10 (IL10) have been shown to be strong inducers of M2 polarization in tumor-associated macrophages (68, 69). Pathway enrichment analysis of genes related to tumor monocyte/macrophage cell communication also suggested an induction of tumor paracrine signaling on macrophage chemotaxis and phenotypic differentiation (Fig. 7A). Multi-IHC revealed that monocytes and macrophages were dominantly located within ACP tissues and exhibited M2 polarization, which would promote an immunosuppressive microenvironment to facilitate tumor progression (Fig. 7B). To further explore the effect of tumors on the functional status of macrophages, we cocultured ACP neoplastic cells with PBMC-derived monocytes/macrophages and THP-1 (a human monocytic cell line) (70). We dissociated ACP tissue and collected neoplastic cells for in vitro culture (Fig. 7C). The results of Western blot showed that monocytes cocultured with neoplastic cell culture medium (CM) exhibited characteristics of macrophage differentiation, for example, the expression of macrophage differentiation markers (*CD11c*, *CD11b*, and *LOX1*) and scavenger receptor (*CD204*) (Fig. 7D). We then focused on the effect of tumor coculture on macrophages polarization. PBMCs and THP-1 were stimulated with phorbol 12-myristate 13-acetate (PMA; 100  $\mu$ M) for 24 hours to be induced into M0 macrophages. First, the quantitative polymerase chain reaction (qPCR) results indicated that cocultured macrophages expressed significantly higher levels of M2 polarization markers (*IL10*, *TGFB1*, *CD163*, *CD206*, and *ARG1*), relative to M1 polarization markers (*TNF*, *IL6*, and *CD86*) (Fig. 7E). Similar results were obtained when detecting the expression of secreted proteins and cell membrane surface markers by ELISA and flow cytometry, respectively (Fig. 7, F and G). Last, the transwell assay revealed that the neoplastic cells cultured in the lower chamber promoted the migration of macrophages in the upper chamber, suggesting that the paracrine effect of neoplastic cells may be involved in the regulatory mechanism of macrophage chemotaxis (Fig. 7H).

### DISCUSSION

Clinically, the outcome of existing treatment for ACP remains unsatisfactory. The tumor heterogeneity of ACP and the complex TME surrounding the outer side of finger-like protrusions have led to therapeutic resistance and tumor recurrence. Hence, a deep understanding of the cell composition and functional characteristics of ACP is urgently needed. In this study, we undertook single-cell transcriptomic analysis and established an atlas of cell maps tailored for ACP tumor tissues, which revealed the characteristics of neoplastic cells and the TME. Our in-depth analysis not only uncovered the phenotypic differences between the TME and normal tissue-derived stromal cells underlying tumor progression but also reconstructed complex cellular communication and molecular networks within the TME.

To date, the molecular characteristics, cell function, dynamics, and plasticity of ACP neoplastic cells are still unclear. The solid part of ACP is composed mainly of PE, stellate cells, and whorl-like cell clusters, which reflects the complicated composition of ACP neoplastic cells. In this study, we identified 10 subpopulations of neoplastic cells, which were further redefined as four main cell states based on transcriptomic characteristics across tumors,

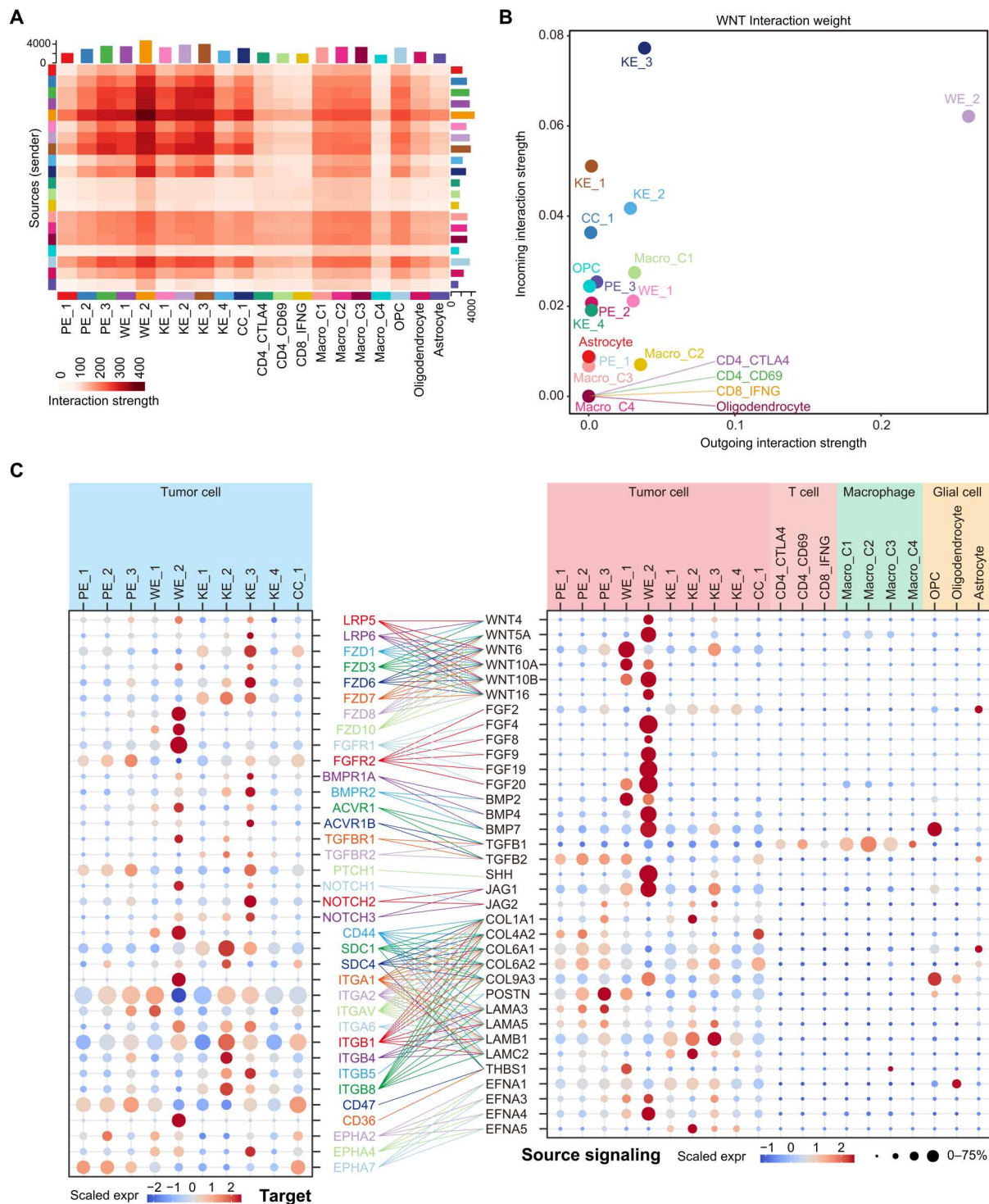


**Fig. 6. Complex cell-cell communication networks in the ACP TME.** (A) Heatmap showing the strength of incoming and outgoing events in interactions between different clusters in the ACP. Histograms separately count the overall intensity of outgoing (y axis) and incoming (x axis) events for each cluster. (B) Interaction strength of WNT signaling pathway incoming and outgoing events between all clusters in ACP. (C) Dot plots show gene expression levels of receptor-ligand pairs involved in interactions between different clusters in ACP.

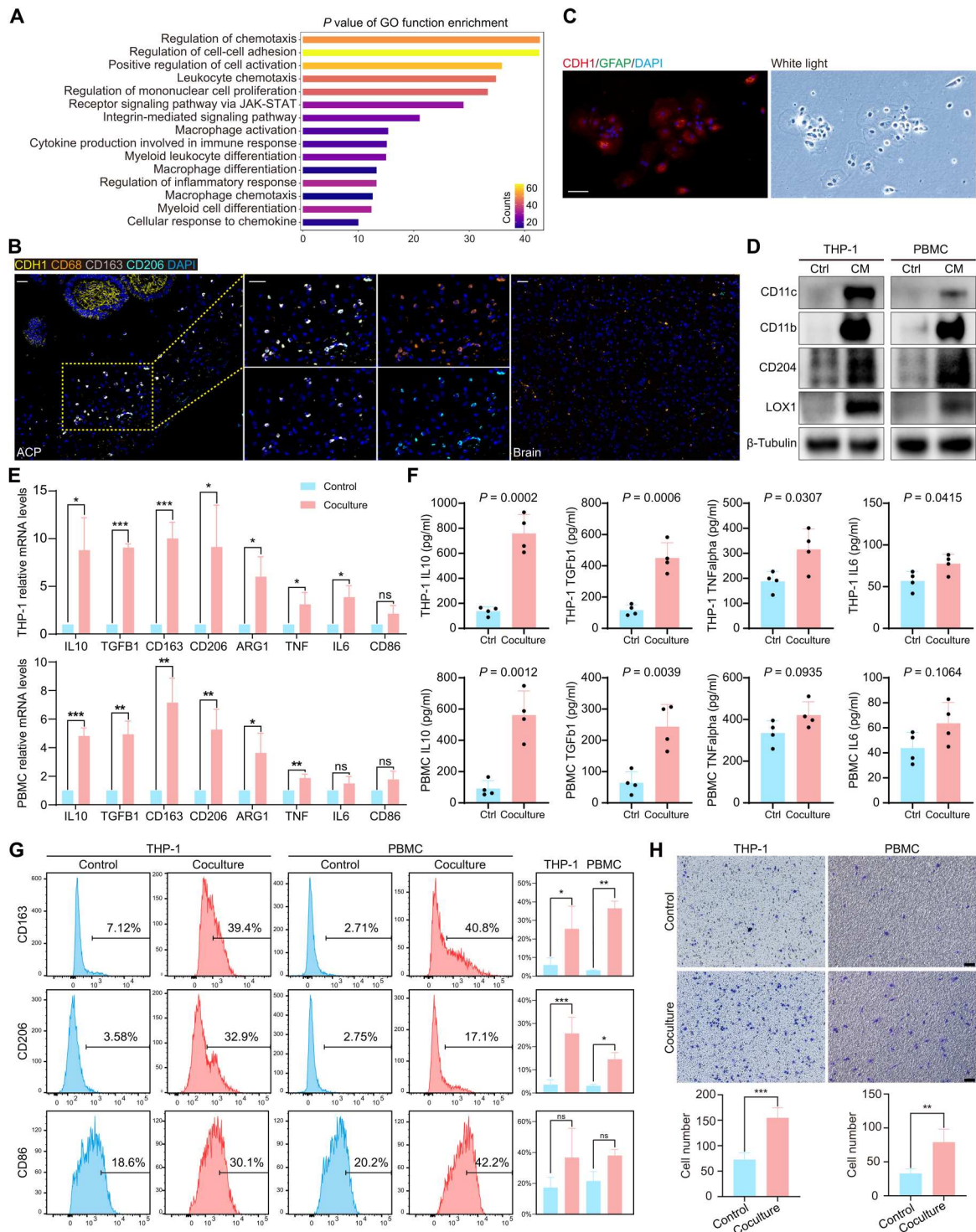


**Fig. 7. Coculture with ACP neoplastic cells induced M2 polarization of macrophages.** (A) GO enrichment analysis of genes involved in tumor monocyte/macrophage intercellular communication. The filled color indicates the number of genes involved in the pathways, and the length of the column indicates the *P* value. (B) Multi-IHC detection of the distribution of M2 phenotype macrophages in the TME. Scale bars, 50  $\mu$ m. (C) Identification of dissociated primary ACP neoplastic cells by immunofluorescence. According to previous sequencing results, CDH1 was used as the positive marker, and GFAP was used as the negative marker. Scale bars, 20  $\mu$ m. (D) After coculture of THP-1 and PBMC with ACP neoplastic cells, the protein expression of macrophage differentiation marker (CD11c, CD11b, CD204, and LOX1) was detected by Western blot. (E) Detection of mRNA levels of M1 (*TNF*, *IL6*, and *CD86*) and M2 (*IL10*, *TGFb1*, *CD163*, *CD206*, and *ARG1*) polarization marker genes in THP-1 and PBMC-derived macrophages by qPCR assay. (F) Detection of cytokine expression levels in cell supernatants in THP-1 and PBMC-derived macrophages by ELISA. (G) The expression levels of cell surface polarization marker proteins in THP-1- and PBMC-derived macrophages were detected by flow cytometry. (H) Transwell assay was used to detect the ability of macrophages in the upper chamber to migrate to the lower chamber. Scale bars, 50  $\mu$ m. \**P* < 0.05, \*\**P* < 0.01, and \*\*\**P* < 0.001. ns, not significant.

including PE, WE, KE, and CC. Different from the growth mode of neoplastic cells infiltrating each other in most solid tumors, these main neoplastic cell states of ACP were characterized by independent histological localization and notable differences in cell morphology and polarity, which suggests that they had different molecular characteristics and cellular kinetics. PE was distributed mainly along the outermost side of finger-like protrusions and was immediately adjacent to reactive glial scars. Neoplastic cells in PE highly expressed genes involved in the early response to stress stimuli, which may be related to their response to the extensive inflammatory environment in glial scar tissues. In addition, two other neoplastic cell states, KE and WE, were distributed mainly medial to the PE in the tumor tissue area. KE had a specific expression profile of keratins, such as cytokeratin *KRT6*, *KRT7*, and *KRT13* and hair follicle keratin *KRT75*, suggesting that they represented a more mature and unique neoplastic cell population at the stage of epithelial development. WE was distributed in the whorl-like structures inside the finger-like protrusions, which was characterized mainly by persistent activation of the WNT signaling pathway. Furthermore, we observed that WE secreted multiple cytokines, such as FGF4, FGF8, BMP2, BMP4, and SHH, which were regulated by the WNT signaling and were previously reported to contribute to the tumorigenesis and development of ACP. These indications suggest that WE tended to act as a functional core and were critical in ACP tumor progression, corroborating the views of previous studies (19, 42). On the basis of tissue structure and gene expression profiling, early studies suggested that tumorigenesis and progression of ACP may be related to the development of ectopic ectoderm (71, 72). It is worth mentioning that although WE and KE are widely distributed in ACP tissues and have distinct biological phenotypes, both of them exhibit lower proliferative activity compared to PE. Meanwhile, transcriptome splicing kinetics and pseudotime analysis revealed distinct evolutionary trajectories of WE and KE in ACP neoplastic cells. Consistent with previous study, only WE among the four cell states showed nuclear accumulation of  $\beta$ -catenin and activation of transcriptional regulatory networks downstream of the WNT pathway, although the vast majority of neoplastic cells harbored activating mutations of *CTNNB1* that drive ACP tumorigenesis (22). In general, *CTNNB1* exon 3 mutations promote nuclear accumulation of  $\beta$ -catenin by preventing its phosphorylation-dependent degradation (73). However, the widespread distribution of membrane-localized  $\beta$ -catenin implied that *CTNNB1* mutation did not appear to be a sufficient condition for the nuclear accumulation of  $\beta$ -catenin and WNT signaling activation in ACP neoplastic cells. Relative to other neoplastic cells, WE present a cellular state that seems like more favorable for nuclear translocation and nuclear homeostasis of  $\beta$ -catenin. We observed that MUC1, a novel biomarker of WE, exhibited cell-wise colocalization with nuclear accumulation of  $\beta$ -catenin. Previous studies have shown that the cytoplasmic tail of MUC1 is capable of binding to  $\beta$ -catenin and promoting steady-state levels of nuclear  $\beta$ -catenin (74, 75). Furthermore, MUC1 bound to  $\beta$ -catenin would inhibit GSK3 $\beta$ -mediated phosphorylation and downstream degradation of  $\beta$ -catenin by acting as competitive substrates (76). Because of off-target effects, inhibitors targeting  $\beta$ -catenin mutations have not been incorporated into the current clinical treatment options for ACP (7). However, WE is still the most promising clinical therapeutic target for ACP. Considering the regulatory role of WE as a paracrine hub for multiple cytokines on the development of

other neoplastic cell states, targeting WE may interfere with the signaling cross-talk within ACP and inhibit tumor progression. In addition, because of the active proliferative capacity, PE may be another potential clinical therapeutic target for precision medicine in ACP.

The progression of ACP is accompanied by the formation of glial scar, which causes local immune cell infiltration. In terms of T cell function in the TME, CD4<sup>+</sup> and CD8<sup>+</sup> T cells showed strong expression of tissue resident markers such as *CD69* and *ITGAE* as well as varying degrees of immune depletion. Tumor-infiltrating T<sub>regs</sub> widely express immune checkpoints such as *CTLA4*, *TIGIT*, and *PDCD1*, suggesting that they may mediate an immunosuppressive microenvironment. Limited by inflammatory or postoperative adhesions, intracystic IFN- $\alpha$  therapy has been used in the management of patients with recurrent ACP. Notably, ICB targeting PD-1 and CTLA-4 has been proposed to produce synergistic effects with IFN- $\alpha$  therapy (77). Combining ICB therapy plus IFN therapy is expected to be a promising nonsurgical treatment for the clinical management of patients with ACP. Macrophages represent the most abundant immune cell type in the TME of ACP and are involved in the regulation of inflammation levels. We found that unlike the classic model of M1-M2 polarization, ACP-infiltrated macrophages exhibited M1-M2 coupled activation, which was reported in previous studies of nasopharyngeal carcinoma and breast cancer (78, 79). This activation mode of macrophages may lead to chronic inflammation in the glial scar during the growth and invasion of brain tissue by ACP. Furthermore, it may be the pathological basis of damage caused by ACP to the hypothalamus and pituitary function, which should be considered for tumor treatment and brain function maintenance.

Reactive glial scars surround the outside of ACP neoplastic cells, constituting their unique tissue microenvironment. They may play a role in tumor progression, which was not elucidated in previous studies. One of the characteristics of glial scars is the activation of astrocytes. Affected by local chronic inflammation and tumor invasion, astrocytes exhibited larger GFAP-positive glial fibers than those in normal brain tissues. Their cell morphology and polarity are changed and arranged in a staggered manner. When the tumor invades the brain, the glial scars act as a buffer area in the organization process. Although we did not detect neurons, this area is enriched by a large number of OLs, possibly the result of migration of OLs induced by the paracrine effects of the tumor, suggesting that the infiltrating OLs in the TME may be involved in promoting tumor progression. It is worth noting that we discovered a cluster of OLs with immune characteristics (iOLs), which is manifested mainly by the expression of immune cell markers related to antigen presentation, such as HLA-DR and CD74. MHC-II components are usually expressed in professional antigen-presenting cells such as dendritic cells and macrophages. Previous studies reported this glial-immune dual characteristic OLs and its characteristics in autoimmune disease models such as MS and EAE, which has a molecular phenotype similar to iOLs in the ACP TME (57, 58). In addition, ACP-derived iOLs have more unique characteristics, which are possibly influenced by tumor paracrine signaling. For example, abundant expression of proteoglycan-dominated extracellular matrix genes may contribute to tumor migration and invasion, indicative of a unique functional transformation of the oligodendrocyte lineage in tumor tissues.

In summary, our research constructed a cellular atlas of ACP neoplastic cells and the tissue microenvironment and described their characteristics and interconnected molecular networks. This study will not only provide a solid foundation for further studies that aim to reveal the cellular and molecular basis of tumorigenesis and progression of ACP but also provide valuable resources for potential clinical treatment and drug development.

## MATERIALS AND METHODS

### ACP samples and normal glial tissue

The study was approved by the Institutional Review Board of West China Hospital of Sichuan University (file no. 20211047A). All samples were collected at West China Hospital of Sichuan University, and informed consent was obtained from all patients. We recruited three patients who were pathologically identified as having ACP for single-cell sequencing (table S1). None of the patients had received radiotherapy, chemotherapy, or other forms of antitumor therapy before surgery. The aggressiveness of ACP causes the tumor and glial tissue to adhere seriously. Fresh ACP tumor tissue and adjacent glial tissue were obtained immediately after surgical resection. Before participating, all patients signed an informed consent form, and all research processes were conducted under the regulations of the Declaration of Helsinki.

### Tissue dissociation and single-cell suspension preparation

Fresh surgical specimens were cut into 1- to 2-mm<sup>3</sup> cubes in a petri dish and rinsed with prechilled Dulbecco's phosphate-buffered saline (DPBS) three times to remove blood clots. The tissue block was incubated with a digestion solution made of 0.1% collagenase IV and 0.1% papain, shaken, and digested in a 37°C constant temperature water bath for 30 min. The digestion juice was shaken gently every 3 to 5 min. When no obvious large pieces of tissue remained, the digestion solution was filtered through a 70- $\mu$ m cell sieve and then through a 40- $\mu$ m cell sieve again, and the filtrate was collected into a new centrifuge tube. The filtrate was centrifuged at 250g for 5 min, the supernatant was discarded, and the cells were washed three times with precooled DPBS. Then, the cell pellet was resuspended in 1 ml of precooled red blood cell lysate and incubated in a 4°C refrigerator with shaking for 15 min. Then, 10 ml of precooled DPBS was added and centrifuged at 250g for 5 min. The cell pellet was resuspended in 3 ml of DPBS without calcium and magnesium ions. The cells were counted with the Countess II Automated Cell Counter. Ten-microliter cell suspension was stained with trypan blue to evaluate cell viability.

### Droplet-based scRNA-seq library preparation

According to the manufacturer's instructions, the Chromium Single Cell 3' Library and Gel Bead and Multiplex Kit (10X Genomics, V3) were used to encapsulate single cells into droplets to construct scRNA-seq libraries. In short, the single-cell suspension with viability higher than 90% was loaded into the Chromium Single-Cell Controller Instrument (10X Genomics) to generate single-cell gel beads in emulsions. Approximately 15,000 cells were added to each channel, aiming to capture 5000 to 10,000 cells per sample. Next, reverse transcription (RT) cleanup, cDNA amplification, and library quality assessment were performed according to the instructions of the kit. The scRNA-seq library was sequenced on the

Illumina NovaSeq 6000 platform to generate 150-bp paired-end reads.

### Preprocessing of scRNA-seq data

Cell Ranger (10X Genomics, 3.0.1) was used to map the sequencing data to the human reference genome (hg38). The scCancer package (2.2.1) based on R software (4.0.5) was used to perform quality control on sequencing data and filter low-quality cells based on the ratio of mitochondrial/ribosomal genes and dissociation-associated genes. The expression matrices of all samples were converted into Seurat objects through the Seurat package (4.0.0). To eliminate the potential impact of double cells on the results, we used the DoubletFinder package (2.0.3) and integrated the factors of gene number and unique molecular identifier (UMI) number to filter the cells. Last, we retained 27,696 high-quality single cells for downstream analysis.

### Integration, dimensionality reduction, clustering, and cell annotation

To eliminate the batch effect, different samples were integrated through the default parameters of the "FindIntegrationAnchors" and "IntegrateData" functions in the Seurat package. Subsequently, to better reflect the biological functional characteristics of the cells, we used the "NormalizeData" function to normalize the expression matrix and the "FindVariableFeatures" function to determine the set of intercellular variant genes in the dataset as highly variable genes (HVGs). To perform dimensionality reduction and clustering on the expression matrix, we used "ScaleData" to scale the data, and "RunPCA" was used to analyze the first 50 main components of the expression matrix. Subsequently, "FindNeighbors" and "FindClusters" were used to cluster the first 25 main components and project them to two-dimensional Uniform Manifold Approximation and Projection (UMAP) or *t*-distributed stochastic neighbor embedding images for display. The characteristic genes of each cell subgroup were calculated through the built-in "FindAllMarkers" function of the Seurat package, and then the cell type of each subgroup was defined on the basis of the SingleR package and the recognized cell marker genes in previous studies.

### CNV analysis and neoplastic cells identification

To identify neoplastic and nonneoplastic cells, we used the inferCNV package (1.6.0) based on R software to calculate the CNV pattern in single cells. The default parameters and clusters composed of immune cells were used as a reference to infer real neoplastic cells. As a verification of the inference results, the expression levels of ACP tumor marker genes obtained based on bulk RNA-seq in previous studies were detected in each cell cluster. The clonality tree was generated using the UPhyloplot2 algorithm (v2.3) to analyze subclonal patterns in ACP (<https://github.com/harbourlab/UPhyloplot2>).

### NMF analysis of the sample heterogeneity expression signatures

For neoplastic cells and oligodendrocyte lineages in ACP, NMF was performed to identify variable expression signatures based on the NMF package (0.23.0). For each sample, we reserved the first 2000 HVGs for the analysis of the expression program in the sample. All negative values in the expression matrix were replaced with 0. For neoplastic cells, we lastly extracted 25 potential

expression signatures from three ACP tumors (table S3). For the oligodendrocyte lineages, 10 expression signatures were extracted (table S7). To study the common characteristics of ACP across samples, we used the R AUCell package to calculate the score of each program in each tumor and then performed hierarchical clustering of all signatures and calculated the Pearson index. In the end, four meta-signatures across tumors were identified, representing the cell cycle, WNT signaling pathway, epithelial differentiation, and stress. For the determination of neoplastic cell states, we used the built-in "AddModuleScore" function of the Seurat package to score the function of single cells. The scoring gene set comes from the four meta-signature marker genes (table S4).

### Gene set variation analysis

The GSVA package (1.38.2) was used to perform pathway enrichment analysis based on scRNA-seq data. The pathways used in the enrichment analysis [including gene ontology (GO), HallMark, and Kyoto Encyclopedia of Genes and Genomes pathways] and the corresponding gene sets were derived mainly from the MSigDB database.

### TF regulatory network analysis

The SCENIC package (1.2.4) was used to construct a TF regulatory network in scRNA-seq data and identify the functional status of cells. To examine differences in the activity of TFs and their downstream target genes across cell clusters, we performed SCENIC analysis on all single cells. The quantification matrix of TF activity was imported into the Seurat object, and subgroup-specific TFs were found via the "FindAllMarkers" function.

### RNA velocity and pseudotime analysis

scVelo (0.2.4) was used to perform RNA velocity analysis to explore the potential evolutionary relationship between cell subpopulations. All parameters were set to default values, and the RNA velocity results were mapped to UMAP images. On the basis of the different trajectories displayed by the RNA velocity results, the corresponding cell subpopulations were extracted, and Monocle3 pseudotime sequence analysis was performed separately. The analysis results of Monocle3, including the pseudotime score and trajectory, were projected onto the UMAP graph of dimensionality reduction and clustering. The "plot\_genes\_in\_pseudotime" function was used to display the genes with notable differences in the pseudotime trajectory.

### Immune cell function status score

We summarized the list of characteristic genes that define T cell functions (such as cytotoxicity, depletion, naïve cells,  $T_{reg}$ s, and tissue retention; table S5) and macrophage functions (such as M1 and M2 polarization; table S6) in published studies. The scoring of cell function based on a specific gene set was performed through the built-in "AddModuleScore" function of the Seurat package.

### Cell-cell communication network

We used CellChat (1.0.0), a database that can accurately analyze cell-cell signal connections and build communication networks, to explore potential cell-cell interactions in the ACP TME. By using the default parameters and the ligand-receptor pair database, if cell type A expresses the ligand that is paired with the receptor

expressed by cell type B, then the event is regarded as a valid interaction. According to the molecular characteristics of the ligand-receptor pair, the interaction events are divided into secretory signals, cell-cell contact, and ECM receptors. We paid particular attention to the potential communication relationships between tumor cell subgroups, tumor immune cells, and tumor glial cells. Communication events between different cell types were displayed in the form of connecting lines.

### IHC and immunofluorescence

The tissue samples were immersed in formalin and fixed for 24 to 48 hours immediately after surgical resection. The tissues were subsequently dehydrated, embedded in paraffin, and sectioned according to the usual procedures. The paraffin sections were baked in an oven at 65°C for 2 hours and then dewaxed and hydrated with xylene and gradient alcohol. EDTA buffer (pH 9.0) or sodium citrate buffer (pH 6.0) was used for antigen retrieval. The sections were preincubated with antibody diluent to seal the nonspecific antibody binding sites of the tissue and then incubated with the primary antibody and secondary antibody sequentially according to the experimental protocol. A PerkinElmer Multiplex IHC staining kit was used for multi-IHC staining according to the manufacturer's instructions. After incubating the primary antibody, the slide was incubated with the secondary antibody, and tyrosine signal amplification was performed. Subsequently, the sections were subjected to microwave heat repair, and the next round of staining was performed. After all the indicators were stained, 4',6-diamidino-2-phenylindole was used to mark the nucleus. Vectra Polaris (PerkinElmer) and Qupath (0.3.0) were used for multispectral slice scanning and image analysis. All antibody information is included in the Supplementary Materials (table S8).

### Isolation of PBMCs

Peripheral blood from patients with ACP was anticoagulated with heparin after collection. Peripheral blood was subjected to density gradient centrifugation with mononuclear cell separation solution (Haoyang, China) to obtain PBMCs. After incubating peripheral blood mononuclear cells with FITC-CD14 monoclonal antibody, flow cytometry was performed to obtain purified CD14<sup>+</sup> PBMCs.

### Cell culture

Primary ACP cells were cultured in EpiLife medium (Thermo Fisher Scientific), and human keratinocyte growth supplement (Thermo Fisher Scientific) was added. Half of the medium was changed every 48 hours. THP-1 cells and PBMCs were cultured in 1640 medium supplemented with 10% fetal bovine serum. PMS (100 nM, MCE) was used to treat THP-1 cells and PBMCs for 24 hours, and then the medium was changed to induce them to differentiate into nonactivated (M0) macrophages.

### Tumor monocyte/macrophage coculture in vitro

To explore the effect of neoplastic cell paracrine signaling on the functional status of monocytes/macrophages, we collected the supernatant of neoplastic cell culture medium and added it to monocyte/macrophage culture dishes. Half of the medium was changed every 24 hours.

## Flow cytometry

Macrophages were blocked with Fc receptor blocking reagent (BioLegend, #422301) before immunostaining. The cells were incubated with monoclonal antibodies labeled with the following fluorescent dyes and detected by flow cytometry: CD86-FITC (BioLegend, #374203), CD163-Alexa 647 (BioLegend, #326507), CD206-APC (BioLegend, #321109), and CD14-FITC (BioLegend, #325603).

## RNA extraction and real-time quantitative PCR

The extraction of total mRNA, RT, and qPCR were carried out in accordance with the published methods of previous studies. TRIzol (Invitrogen) was used to isolate and extract total mRNA from cells or tissues, and after determining the concentration, the PrimeScript RT reagent Kit (Takara) was used for RT to obtain cDNA. According to the manufacturer's requirements, TB Green Premix Ex Taq II (Takara) was used for qPCR analysis. The amplification step in the PCR consisted of 40 cycles of denaturation (95°C, 15 s) and annealing extension (60°C, 60 s). After the last cycle, all samples were subjected to melting point analysis with a temperature range of 60° to 95°C. Using ACTB as a housekeeping gene, the relative expression value of the gene was calculated. Refer to table S9 for the primer information required for the reaction.

## Western blot

Total protein was collected from cells or tissues with radioimmunoprecipitation assay lysis solution (Thermo Fisher Scientific) and boiled to denature the total protein. The protein concentration was detected using a bicinchoninic acid kit. Protein samples (10 to 20 µg) were run on SDS-polyacrylamide gel electrophoresis gels for electrophoresis. After transferring the protein to the polyvinylidene difluoride membrane, according to the experimental requirements, the membrane was blocked and incubated with the corresponding primary antibody at 4°C for 12 to 16 hours. Subsequently, the membrane was washed three times, after which it was incubated with the horseradish peroxidase-conjugated secondary antibody, and the color reaction was performed with the enhanced chemiluminescence (ECL) kit to detect the Western blot. β-Tubulin was used as a housekeeping gene to evaluate the relative expression value of each index. Refer to table S8 for all antibody information.

## Cytokine detection

According to the manufacturer's specifications, an ELISA kit (R&D Systems) was used to detect the levels of IL4, TGFβ1, IL12, and tumor necrosis factor-α in the supernatant of macrophages. IFN-γ is detected in tumors and brain tissues. Standards with different concentration gradients were tested to construct a standard curve by the four-parameter logistic fitting curve method.

## Cell migration experiment

Transwell chambers (Corning, catalog no. 3422) with 8-µm pores were used to detect the migration of macrophages. In short,  $1 \times 10^4$  M0 macrophages (from THP-1 cells and PBMCs pretreated with PMA for 24 hours) were seeded in the upper chambers, and  $1 \times 10^4$  ACP primary neoplastic cells were placed in the lower chambers. The culture plate was placed in a 37°C incubator for 48 hours, and then the transwell chambers were removed and fixed with 4% paraformaldehyde. After staining the chambers with crystal violet, a moistened cotton swab was used to carefully wipe away the

remaining cells inside the chambers. A microscope was used to observe and count the cells that migrated on the bottom surface of the chambers.

## Statistical analysis

Data statistics are performed based on GraphPad Prism 8.0 software. We obtained the *P* value of the difference between different groups by performing Student's *t* test and one-way analysis of variance (ANOVA). When *P* < 0.05, differences were considered statistically significant.

## Supplementary Materials

This PDF file includes:

Figs. S1 to S12

Legends for tables S1 to S9

Other Supplementary Material for this manuscript includes the following:

Tables S1 to S9

[View/request a protocol for this paper from Bio-protocol.](#)

## REFERENCES AND NOTES

- H. L. Muller, Childhood craniopharyngioma—current concepts in diagnosis, therapy and follow-up. *Nat. Rev. Endocrinol.* **6**, 609–618 (2010).
- H. L. Muller, Craniopharyngioma. *Endocr. Rev.* **35**, 513–543 (2014).
- J. Muller-Scholden, T. Lehrnbecher, H. L. Müller, J. Bensch, R. H. Hengen, N. Sörensen, H. B. Stockhausen, Radical surgery in a neonate with craniopharyngioma. report of a case. *Pediatr. Neurosurg.* **33**, 265–269 (2000).
- W. Bailey, G. R. Freidenberg, H. E. James, J. R. Hesselink, K. L. Jones, Prenatal diagnosis of a craniopharyngioma using ultrasonography and magnetic resonance imaging. *Prenat. Diagn.* **10**, 623–629 (1990).
- F. Chentli, F. Belhimer, F. Kessaci, B. Mansouri, Congenital craniopharyngioma: A case report and literature review. *J. Pediatr. Endocrinol. Metab.* **25**, 1181–1183 (2012).
- H. L. Muller, T. E. Merchant, M. Warmuth-Metz, J. P. Martinez-Barbera, S. Puget, Craniopharyngioma. *Nat. Rev. Dis. Primers.* **5**, 75 (2019).
- A. C. Hengartner, E. Prince, T. Vijmasi, T. C. Hankinson, Adamantinomatous craniopharyngioma: Moving toward targeted therapies. *Neurosurg. Focus* **48**, E7 (2020).
- H. L. Muller, T. E. Merchant, S. Puget, J.-P. Martinez-Barbera, New outlook on the diagnosis, treatment and follow-up of childhood-onset craniopharyngioma. *Nat. Rev. Endocrinol.* **13**, 299–312 (2017).
- N. Karavitaki, S. Cudlip, C. B. Adams, J. A. Wass, Craniopharyngiomas. *Endocr. Rev.* **27**, 371–397 (2006).
- J. M. Gonzalez-Meljem, J. P. Martinez-Barbera, Adamantinomatous craniopharyngioma as a model to understand paracrine and senescence-induced tumorigenesis. *Cell. Mol. Life Sci.* **78**, 4521–4544 (2021).
- S. J. Larkin, O. Anson, Pathology and pathogenesis of craniopharyngiomas. *Pituitary* **16**, 9–17 (2013).
- C. L. Andoniadou, C. Gaston-Massuet, R. Reddy, R. P. Schneider, M. A. Blasco, P. le Tissier, T. S. Jacques, L. H. Pevny, M. T. Dattani, J. P. Martinez-Barbera, Identification of novel pathways involved in the pathogenesis of human adamantinomatous craniopharyngioma. *Acta Neuropathol.* **124**, 259–271 (2012).
- E. M. Erfurth, Diagnosis, Background, and Treatment of Hypothalamic Damage in Craniopharyngioma. *Neuroendocrinology* **110**, 767–779 (2020).
- J. Yang, Z. Hou, C. Wang, H. Wang, H. Zhang, Gene expression profiles reveal key genes for early diagnosis and treatment of adamantinomatous craniopharyngioma. *Cancer Gene Ther.* **25**, 227–239 (2018).
- A. Gautier, A. Godbout, C. Grosheny, I. Tejedor, M. Coudert, C. Courtillot, C. Jublanc, M. De Kerdanet, J.-Y. Poirier, L. Riffaud, C. Sainte-Rose, R. Van Effenterre, G. Brassier, F. Bonnet, P. Touraine; Craniopharyngioma Study Group, Markers of recurrence and long-term morbidity in craniopharyngioma: A systematic analysis of 171 patients. *J. Clin. Endocrinol. Metab.* **97**, 1258–1267 (2012).
- J. P. Martinez-Barbera, C. L. Andoniadou, Biological Behaviour of Craniopharyngiomas. *Neuroendocrinology* **110**, 797–804 (2020).

17. C. Stache, A. Hölsken, S.-M. Schlaffer, A. Hess, M. Metzler, B. Frey, R. Fahlbusch, J. Flitsch, M. Buchfelder, R. Buslei, Insights into the infiltrative behavior of adamantinomatous craniopharyngioma in a new xenotransplant mouse model. *Brain Pathol.* **25**, 1–10 (2015).
18. S. Sekine, T. Shibata, A. Kokubu, Y. Morishita, M. Noguchi, Y. Nakanishi, M. Sakamoto, S. Hirohashi, Craniopharyngiomas of adamantinomatous type harbor beta-catenin gene mutations. *Am. J. Pathol.* **161**, 1997–2001 (2002).
19. J. R. Apps, G. Carreno, J. M. Gonzalez-Meljem, S. Haston, R. Guiho, J. E. Cooper, S. Manshaei, N. Jani, A. Hölsken, B. Pettorini, R. J. Beynon, D. M. Simpson, H. C. Fraser, Y. Hong, S. Hallang, T. J. Stone, A. Virasami, A. M. Donson, D. Jones, K. Aquilina, H. Spoudeas, A. R. Joshi, R. Grundy, L. C. D. Storer, M. Korbonits, D. A. Hilton, K. Tossell, S. Thavaraj, M. A. Ungless, J. Gil, R. Buslei, T. Hankinson, D. Hargrave, C. Goding, C. L. Andoniadou, P. Brogan, T. S. Jacques, H. J. Williams, J. P. Martinez-Barbera, Tumour compartment transcriptomics demonstrates the activation of inflammatory and odontogenic programmes in human adamantinomatous craniopharyngioma and identifies the MAPK/ERK pathway as a novel therapeutic target. *Acta Neuropathol.* **135**, 757–777 (2018).
20. P. K. Brastianos, A. Taylor-Weiner, P. E. Manley, R. T. Jones, D. Dias-Santagata, A. R. Thorner, M. S. Lawrence, F. J. Rodriguez, L. A. Bernardo, L. Schubert, A. Sunkavalli, N. Shillingford, M. L. Calicchio, H. G. W. Lidov, H. Taha, M. Martinez-Lage, M. Santi, P. B. Storm, J. Y. K. Lee, J. N. Palmer, N. D. Adappa, R. M. Scott, I. F. Dunn, E. R. Laws Jr., C. Stewart, K. L. Ligon, M. P. Hoang, P. van Hummelen, W. C. Hahn, D. N. Louis, A. C. Resnick, M. W. Kieran, G. Getz, S. Santagata, Exome sequencing identifies BRAF mutations in papillary craniopharyngiomas. *Nat. Genet.* **46**, 161–165 (2014).
21. S. Haston, S. Manshaei, J. P. Martinez-Barbera, Stem/progenitor cells in pituitary organ homeostasis and tumorigenesis. *J. Endocrinol.* **236**, R1–R13 (2018).
22. J. R. Apps, C. Stache, J. M. Gonzalez-Meljem, A. Gutteridge, J. Chalker, T. S. Jacques, T. Forshaw, A. Hölsken, J. P. Martinez-Barbera, CTNNB1 mutations are clonal in adamantinomatous craniopharyngioma. *Neuropathol. Appl. Neurobiol.* **46**, 510–514 (2020).
23. D. J. Papke Jr., B. C. Dickson, L. Sholl, C. D. M. Fletcher, Pseudoendocrine Sarcoma: Clinicopathologic analysis of 23 cases of a distinctive soft tissue neoplasm with metastatic potential, recurrent CTNNB1 mutations, and a predilection for truncal locations. *Am. J. Surg. Pathol.* **46**, 33–43 (2022).
24. R. Yaeger, W. K. Chatila, M. D. Lipsyc, J. F. Hechtman, A. Cercek, F. Sanchez-Vega, G. Jayakumar, S. Middha, A. Zehir, M. T. A. Donoghue, D. You, A. Viale, N. Kemeny, N. H. Segal, Z. K. Stadler, A. M. Varghese, R. Kundra, J. Gao, A. Syed, D. M. Hyman, E. Vakiani, N. Rosen, B. S. Taylor, M. Ladanyi, M. F. Berger, D. B. Solit, J. Shia, L. Saltz, N. Schultz, Clinical Sequencing Defines the Genomic Landscape of Metastatic Colorectal Cancer. *Cancer Cell* **33**, 125–136.e3 (2018).
25. J. M. Gonzalez-Meljem, S. Haston, G. Carreno, J. R. Apps, S. Pozzi, C. Stache, G. Kaushal, A. Virasami, L. Panousopoulos, S. N. Mousavy-Gharavy, A. Guerrero, M. Rashid, N. Jani, C. R. Goding, T. S. Jacques, D. J. Adams, J. Gil, C. L. Andoniadou, J. P. Martinez-Barbera, Stem cell senescence drives age-attenuated induction of pituitary tumours in mouse models of paediatric craniopharyngioma. *Nat. Commun.* **8**, 1819 (2017).
26. K. Kato, Y. Nakatani, H. Kanno, Y. Inayama, R. Ijiri, N. Nagahara, T. Miyake, M. Tanaka, Y. Ito, N. Aida, K. Tachibana, K.-I. Sekido, Y. Tanaka, Possible linkage between specific histological structures and aberrant reactivation of the Wnt pathway in adamantinomatous craniopharyngioma. *J. Pathol.* **203**, 814–821 (2004).
27. S. Sekine, T. Takata, T. Shibata, M. Mori, Y. Morishita, M. Noguchi, T. Uchida, Y. Kanai, S. Hirohashi, Expression of enamel proteins and LEF1 in adamantinomatous craniopharyngioma: Evidence for its odontogenic epithelial differentiation. *Histopathology* **45**, 573–579 (2004).
28. C. Martelli, R. Serra, I. Insera, D. V. Rossetti, F. Iavarone, F. Vincenzoni, M. Castagnola, A. Urbani, G. Tamburrini, M. Caldarelli, L. Massimi, C. Desiderio, Investigating the Protein Signature of Adamantinomatous Craniopharyngioma Pediatric Brain Tumor Tissue: Towards the comprehension of its aggressive behavior. *Dis. Markers* **2019**, 3609789 (2019).
29. J. R. Apps, J. C. Hutchinson, O. J. Arthurs, A. Virasami, A. Joshi, B. Zeller-Plumhoff, D. Moulding, T. S. Jacques, N. J. Sebire, J. P. Martinez-Barbera, Imaging invasion: Micro-CT imaging of adamantinomatous craniopharyngioma highlights cell type specific spatial relationships of tissue invasion. *Acta Neuropathol. Commun.* **4**, 57 (2016).
30. S. Burghaus, A. Hölsken, M. Buchfelder, R. Fahlbusch, B. M. Riederer, V. Hans, I. Blümcke, R. Buslei, A tumor-specific cellular environment at the brain invasion border of adamantinomatous craniopharyngiomas. *Virchows Arch.* **456**, 287–300 (2010).
31. Y. Wang, J. Deng, L. Wang, T. Zhou, J. Yang, Z. Tian, J. Yang, H. Chen, X. Tang, S. Zhao, L. Zhou, A. Tong, J. Xu, Expression and clinical significance of PD-L1, B7-H3, B7-H4 and VISTA in craniopharyngioma. *J. Immunother. Cancer* **8**, e000406 (2020).
32. S. Liebner, R. M. Dijkhuizen, Y. Reiss, K. H. Plate, D. Agalliu, G. Constantin, Functional morphology of the blood-brain barrier in health and disease. *Acta Neuropathol.* **135**, 311–336 (2018).
33. P. S. Steeg, The blood-tumour barrier in cancer biology and therapy. *Nat. Rev. Clin. Oncol.* **18**, 696–714 (2021).
34. D. F. Quail, J. A. Joyce, The microenvironmental landscape of brain tumors. *Cancer Cell* **31**, 326–341 (2017).
35. D. Grun, A. van Oudenaarden, Design and analysis of single-cell sequencing experiments. *Cell* **163**, 799–810 (2015).
36. C. Gaston-Massuet, C. L. Andoniadou, M. Signore, S. A. Jayakody, N. Charolidi, R. Kyeyune, B. Vernay, T. S. Jacques, M. M. Taketo, P. Le Tissier, M. T. Dattani, J. P. Martinez-Barbera, Increased Wntless (Wnt) signaling in pituitary progenitor/stem cells gives rise to pituitary tumors in mice and humans. *Proc. Natl. Acad. Sci. U.S.A.* **108**, 11482–11487 (2011).
37. H. Tateyama, T. Tada, M. Okabe, E. Takahashi, T. Eimoto, Different keratin profiles in craniopharyngioma subtypes and ameloblastomas. *Pathol. Res. Pract.* **197**, 735–742 (2001).
38. J. P. Martinez-Barbera, Molecular and cellular pathogenesis of adamantinomatous craniopharyngioma. *Neuropathol. Appl. Neurobiol.* **41**, 721–732 (2015).
39. M. Sato, M. Matsumoto, Y. Saiki, M. Alam, H. Nishizawa, M. Rokugo, A. Brydun, S. Yamada, M. K. Kaneko, R. Funayama, M. Ito, Y. Kato, K. Nakayama, M. Unno, K. Igarashi, BACH1 promotes pancreatic cancer metastasis by repressing epithelial genes and enhancing epithelial-mesenchymal transition. *Cancer Res.* **80**, 1279–1292 (2020).
40. C. Zanduetta, C. Ormazabal, N. Perurena, S. Martinez-Canarias, M. Zalacaín, M. S. Julián, A. E. Grigoriadis, K. Valencia, F. J. Campos-Laborie, J. D. L. Rivas, S. Vicent, A. Patiño-García, F. Lecanda, Matrix-Gla protein promotes osteosarcoma lung metastasis and associates with poor prognosis. *J. Pathol.* **239**, 438–449 (2016).
41. J. P. Martinez-Barbera, C. L. Andoniadou, Concise review: Paracrine role of stem cells in pituitary tumors: A focus on adamantinomatous craniopharyngioma. *Stem Cells* **34**, 268–276 (2016).
42. C. L. Andoniadou, D. Matsushima, S. N. Mousavy Gharavy, M. Signore, A. I. Mackintosh, M. Schaeffer, C. Gaston-Massuet, P. Mollard, T. S. Jacques, P. Le Tissier, M. T. Dattani, L. H. Pevny, J. P. Martinez-Barbera, Sox2(+) stem/progenitor cells in the adult mouse pituitary support organ homeostasis and have tumor-inducing potential. *Cell Stem Cell* **13**, 433–445 (2013).
43. V. M. Ravi, P. Will, J. Kueckelhaus, N. Sun, K. Joseph, H. Salié, L. Vollmer, U. Kuliesiute, J. von Ehr, J. K. Benotmane, N. Neidert, M. Follo, F. Scherer, J. M. Goeldner, S. P. Behringer, P. Franco, M. Khat, J. Zhang, U. G. Hofmann, C. Fung, F. L. Ricklefs, K. Lamszus, M. Boerries, M. Ku, J. Beck, R. Sankowski, M. Schwabenland, M. Prinz, U. Schüller, S. Killmer, B. Bengsch, A. K. Walch, D. Delev, O. Schnell, D. H. Heiland, Spatially resolved multi-omics deciphers bidirectional tumor-host interdependence in glioblastoma. *Cancer Cell* **40**, 639–655.e13 (2022).
44. A. Erickson, M. He, E. Berglund, M. Marklund, R. Mirzazadeh, N. Schultz, L. Kvastad, A. Andersson, L. Bergenstråhle, J. Bergenstråhle, L. Larsson, L. Alonso Galicia, A. Shamikh, E. Basmaci, T. Diaz de Ståhl, T. Rajakumar, D. Doultinos, K. Thrane, A. L. Ji, P. A. Khavari, F. Tarish, A. Tanoglidis, J. Maaskola, R. Colling, T. Mirtti, F. C. Hamdy, D. J. Woodcock, T. Helleday, I. G. Mills, A. D. Lamb, J. Lundeberg, Spatially resolved clonal copy number alterations in benign and malignant tissue. *Nature* **608**, 360–367 (2022).
45. S. Kurtenbach, A. M. Cruz, D. A. Rodriguez, M. A. Durante, J. W. Harbour, Uphyloplot2: Visualizing phylogenetic trees from single-cell RNA-seq data. *BMC Genomics* **22**, 419 (2021).
46. Y. Zhou, D. Yang, Q. Yang, X. Lv, W. Huang, Z. Zhou, Y. Wang, Z. Zhang, T. Yuan, X. Ding, L. Tang, J. Zhang, J. Yin, Y. Huang, W. Yu, Y. Wang, C. Zhou, Y. Su, A. He, Y. Sun, Z. Shen, B. Qian, W. Meng, J. Fei, Y. Yao, X. Pan, P. Chen, H. Hu, Single-cell RNA landscape of intratumoral heterogeneity and immunosuppressive microenvironment in advanced osteosarcoma. *Nat. Commun.* **11**, 6322 (2020).
47. R. Whelan, E. Prince, A. Gilani, T. Hankinson, The inflammatory milieu of adamantinomatous craniopharyngioma and its implications for treatment. *J. Clin. Med.* **9**, 519 (2020).
48. Q. Gao, J. Luo, J. Pan, L. Zhang, D. Song, M. Zhang, D. Xu, F. Guo, Integrative analyses identify HIF-1 $\alpha$  as a potential protective role with immune cell infiltration in adamantinomatous craniopharyngioma. *Front. Immunol.* **13**, 949509 (2022).
49. S. Coy, R. Rashid, J.-R. Lin, Z. du, A. M. Donson, T. C. Hankinson, N. K. Foreman, P. E. Manley, M. W. Kieran, D. A. Reardon, P. K. Sorger, S. Santagata, Multiplexed immunofluorescence reveals potential PD-1/PD-L1 pathway vulnerabilities in craniopharyngioma. *Neuro Oncol.* **20**, 1101–1112 (2018).
50. R. Whelan, A. Hengartner, Z. Folzenlogen, E. Prince, T. C. Hankinson, Adamantinomatous craniopharyngioma in the molecular age and the potential of targeted therapies: A review. *Childs Nerv. Syst.* **36**, 1635–1642 (2020).
51. X. Guo, Y. Zhang, L. Zheng, C. Zheng, J. Song, Q. Zhang, B. Kang, Z. Liu, L. Jin, R. Xing, R. Gao, L. Zhang, M. Dong, X. Hu, X. Ren, D. Kirchhoff, H. G. Roeder, T. Yan, Z. Zhang, Global characterization of T cells in non-small-cell lung cancer by single-cell sequencing. *Nat. Med.* **24**, 978–985 (2018).
52. L. Massimi, C. Martelli, M. Caldarelli, M. Castagnola, C. Desiderio, Proteomics in pediatric cystic craniopharyngioma. *Brain Pathol.* **27**, 370–376 (2017).
53. M. Liu, Z. Tong, C. Ding, F. Luo, S. Wu, C. Wu, S. Albeituni, L. He, X. Hu, D. Tieri, E. C. Rouchka, M. Hamada, S. Takahashi, A. A. Gibb, G. Kloecker, H.-G. Zhang, M. Bousamra II, B. G. Hill,

- X. Zhang, J. Yan, Transcription factor c-Maf is a checkpoint that programs macrophages in lung cancer. *J. Clin. Invest.* **130**, 2081–2096 (2020).
54. T. Ullmann, S. Luckhardt, M. Wolf, M. J. Parnham, E. Resch, High-throughput screening for CEBPD-modulating compounds in THP-1-derived reporter macrophages identifies anti-inflammatory HDAC and BET inhibitors. *Int. J. Mol. Sci.* **22**, 3022 (2021).
55. X. Li, M. Li, L. Tian, J. Chen, R. Liu, B. Ning, Reactive astrogliosis: Implications in spinal cord injury progression and therapy. *Oxid. Med. Cell. Longev.* **2020**, 9494352 (2020).
56. M. Linnerbauer, V. Rothhammer, Protective functions of reactive astrocytes following central nervous system insult. *Front. Immunol.* **11**, 573256 (2020).
57. S. Jäkel, E. Agirre, A. M. Falcão, D. van Bruggen, K. W. Lee, I. Knuesel, D. Malhotra, C. Ffrench-Constant, A. Williams, G. Castelo-Branco, Altered human oligodendrocyte heterogeneity in multiple sclerosis. *Nature* **566**, 543–547 (2019).
58. A. M. Falcao, D. van Bruggen, S. Marques, M. Meijer, S. Jäkel, E. Agirre, E. M. F. Samudiyata, D. P. Vanichkina, C. Ffrench-Constant, A. Williams, A. O. Guerreiro-Cacais, G. Castelo-Branco, Disease-specific oligodendrocyte lineage cells arise in multiple sclerosis. *Nat. Med.* **24**, 1835–1844 (2018).
59. L. Kirby, J. Jin, J. G. Cardona, M. D. Smith, K. A. Martin, J. Wang, H. Strasburger, L. Herbst, M. Alexis, J. Karnell, T. Davidson, R. Dutta, J. Goverman, D. Bergles, P. A. Calabresi, Oligodendrocyte precursor cells present antigen and are cytotoxic targets in inflammatory demyelination. *Nat. Commun.* **10**, 3887 (2019).
60. L. Schirmer, D. P. Schafer, T. Bartels, D. H. Rowitch, P. A. Calabresi, Diversity and function of glial cell types in multiple sclerosis. *Trends Immunol.* **42**, 228–247 (2021).
61. C. Neftel, J. Laffy, M. G. Filbin, T. Hara, M. E. Shore, G. J. Rahme, A. R. Richman, D. Silverbush, M. L. Shaw, C. M. Hebert, J. Dewitt, S. Gritsch, E. M. Perez, L. N. Gonzalez Castro, X. Lan, N. Druck, C. Rodman, D. Dionne, A. Kaplan, M. S. Bertalan, J. Small, K. Pelton, S. Becker, D. Bonal, Q.-D. Nguyen, R. L. Servis, J. M. Fung, R. Mylvaganam, L. Mayr, J. Gojo, C. Haberler, R. Geyeregger, T. Czech, I. Slavic, B. V. Nahed, W. T. Curry, B. S. Carter, H. Wakimoto, P. K. Brastianos, T. T. Batchelor, A. Stemmer-Rachamimov, M. Martinez-Lage, M. P. Frosch, I. Stamenkovic, N. Riggi, E. Rheinbay, M. Monje, O. Rozenblatt-Rosen, D. P. Cahill, A. P. Patel, T. Hunter, I. M. Verma, K. L. Ligon, D. N. Louis, A. Regev, B. E. Bernstein, I. Tirosh, M. L. Suvà, An integrative model of cellular states, plasticity, and genetics for glioblastoma. *Cell* **178**, 835–849.e21 (2019).
62. Y. Zhang, X. Zou, W. Qian, X. Weng, L. Zhang, L. Zhang, S. Wang, X. Cao, L. Ma, G. Wei, Y. Wu, Z. Hou, Enhanced PAPSS2/VCAN sulfation axis is essential for Snail-mediated breast cancer cell migration and metastasis. *Cell Death Differ.* **26**, 565–579 (2019).
63. Q. Zhang, J. Wu, X. Chen, M. Zhao, D. Zhang, F. Gao, Upregulation of versican associated with tumor progression, metastasis, and poor prognosis in bladder carcinoma. *Biomed. Res. Int.* **2021**, 6949864 (2021).
64. Y.-J. Chen, J.-X. Zhang, L. Shen, Q. Qi, X.-X. Cheng, Z.-R. Zhong, Z.-Q. Jiang, R. Wang, H.-Z. Lü, J.-G. Hu, Schwann cells induce proliferation and migration of oligodendrocyte precursor cells through secretion of PDGF-AA and FGF-2. *J. Mol. Neurosci.* **56**, 999–1008 (2015).
65. J.-G. Hu, X.-J. Wu, Y.-F. Feng, G.-M. Xi, Z.-H. Wang, J.-S. Zhou, H.-Z. Lü, PDGF-AA and bFGF mediate B104CM-induced proliferation of oligodendrocyte precursor cells. *Int. J. Mol. Med.* **30**, 1113–1118 (2012).
66. M. Neri, C. Maderna, D. Ferrari, C. Cavazzin, A. L. Vescovi, A. Gritti, Robust generation of oligodendrocyte progenitors from human neural stem cells and engraftment in experimental demyelination models in mice. *PLOS ONE* **5**, e10145 (2010).
67. G. Karpathiou, M. Hamlat, M. Dridi, F. Forest, A. Papoudou-Bai, J. M. Dumollard, M. Peoch, Autophagy and immune microenvironment in craniopharyngioma and ameloblastoma. *Exp. Mol. Pathol.* **123**, 104712 (2021).
68. A. N. Gordon-Weeks, S. Y. Lim, A. E. Yuzhalin, K. Jones, R. Muschel, Macrophage migration inhibitory factor: A key cytokine and therapeutic target in colon cancer. *Cytokine Growth Factor Rev.* **26**, 451–461 (2015).
69. M. Barbosa de Souza, M. B. de Carvalho, E. J. Kim, B. E. Rendon, J. T. Noe, A. D. Wise, R. A. Mitchell, Oral squamous carcinoma cells promote macrophage polarization in an MIF-dependent manner. *QJM* **111**, 769–778 (2018).
70. W.-C. Huang, K.-T. Kuo, C.-H. Wang, C.-T. Yeh, Y. Wang, Cisplatin resistant lung cancer cells promoted M2 polarization of tumor-associated macrophages via the Src/CD155/MIF functional pathway. *J. Exp. Clin. Cancer Res.* **38**, 180 (2019).
71. S. Manjila, N. E. Asmar, B. M. Vidalis, F. Alonso, G. Singh, K. Vadamalai, M. L. Cohen, N. C. Bambakidis, B. M. Arafah, W. R. Selman, Intratumoral Rathke's cleft cyst remnants within craniopharyngioma, pituitary adenoma, suprasellar dermoid, and epidermoid cysts: A ubiquitous signature of ectodermal lineage or a transitional entity? *Neurosurgery* **85**, 180–188 (2019).
72. M. J. Harrison, S. Morgello, K. D. Post, Epithelial cystic lesions of the sellar and parasellar region: A continuum of ectodermal derivatives? *J. Neurosurg.* **80**, 1018–1025 (1994).
73. Y. Zhang, X. Wang, Targeting the Wnt/ $\beta$ -catenin signaling pathway in cancer. *J. Hematol. Oncol.* **13**, 165 (2020).
74. Y. Wen, T. C. Caffrey, M. J. Wheelock, K. R. Johnson, M. A. Hollingsworth, Nuclear association of the cytoplasmic tail of MUC1 and beta-catenin. *J. Biol. Chem.* **278**, 38029–38039 (2003).
75. S. E. Baldus, S. P. Mönig, S. Huxel, S. Landsberg, F.-G. Hanisch, K. Engelmann, P. M. Schneider, J. Thiele, A. H. Hölscher, H. P. Dienes, MUC1 and nuclear beta-catenin are coexpressed at the invasion front of colorectal carcinomas and are both correlated with tumor prognosis. *Clin. Cancer Res.* **10**, 2790–2796 (2004).
76. L. Huang, D. Chen, D. Liu, L. Yin, S. Kharbanda, D. Kufe, MUC1 oncoprotein blocks glycogen synthase kinase 3 $\beta$ -mediated phosphorylation and degradation of beta-catenin. *Cancer Res.* **65**, 10413–10422 (2005).
77. B. Hu, M. Yu, X. Ma, J. Sun, C. Liu, C. Wang, S. Wu, P. Fu, Z. Yang, Y. He, Y. Zhu, C. Huang, X. Yang, Y. Shi, S. Qiu, H. Sun, A. X. Zhu, J. Zhou, Y. Xu, D. Zhu, J. Fan, IFN $\alpha$  potentiates anti-PD-1 efficacy by remodeling glucose metabolism in the hepatocellular carcinoma microenvironment. *Cancer Discov.* **12**, 1718–1741 (2022).
78. S. Jin, R. Li, M.-Y. Chen, C. Yu, L.-Q. Tang, Y.-M. Liu, J.-P. Li, Y.-N. Liu, Y.-L. Luo, Y. Zhao, Y. Zhang, T.-L. Xia, S.-X. Liu, Q. Liu, G.-N. Wang, R. You, J.-Y. Peng, J. Li, F. Han, J. Wang, Q.-Y. Chen, L. Zhang, H.-Q. Mai, B. E. Gewurz, B. Zhao, L. S. Young, Q. Zhong, F. Bai, M.-S. Zeng, Single-cell transcriptomic analysis defines the interplay between tumor cells, viral infection, and the microenvironment in nasopharyngeal carcinoma. *Cell Res.* **30**, 950–965 (2020).
79. E. Azizi, A. J. Carr, G. Plitas, A. E. Cornish, C. Konopacki, S. Prabhakaran, J. Nainys, K. Wu, V. Kiseliovas, M. Setty, K. Choi, R. M. Fromme, P. Dao, P. T. M. Kenney, R. C. Wasti, K. Kadaveru, L. Mazutis, A. Y. Rudensky, D. Pe'er, Single-cell map of diverse immune phenotypes in the breast tumor microenvironment. *Cell* **174**, 1293–1308.e36 (2018).

**Acknowledgments:** We are grateful to Shanghai Biotechnology Corporation for assistance in scRNA-seq. We are grateful to X. Cheng, Y. Zhang, and S. Jizhi of Medical Corporation for assistance in scRNA-seq personalized statistical consultation. We also thank C. Bao and F. Chen from the Institute of Clinical Pathology, West China Hospital of Sichuan University, for the technical support in histological staining. **Funding:** This work was supported by the 1.3.5 project for disciplines of excellence, West China Hospital, Sichuan University (ZYJC18007), National Natural Science Foundation of China (82173175 and 31771549), and key research and development project of science and technology department of Sichuan Province (2019YF50392). **Author contributions:** Conceptualization: Y.J., J.Y., and R.L. Data curation: Y.J. Formal analysis: Y.J. Funding acquisition: Y.C. and J.X. Investigation: Y.J., J.Y., X.Z., R.F., B.S., H.L., L.L., M.W., X.Q., H.C., Q.R., Z.L., Y.W., J.Z., P.Z., Q.L., M.T., J.Y., C.W., X.L., S.J., and L.Z. Methodology: Y.J., G.Z., Y.C., and Y.W. Project administration: Y.J., J.Y., R.L., and J.X. Resources: Y.J., J.Y., and X.Z. Supervision: G.Z., Y.C., and J.X. Validation: Y.J., J.Y., L.L., and X.Q. Visualization: Y.J. Writing—original draft: Y.J., G.Z., and Y.C. Writing—review and editing: Y.J., G.Z., and Y.C. **Competing interests:** The authors declare that they have no competing interests. **Data and materials availability:** All data needed to evaluate the conclusions in the paper are present in the paper and/or the Supplementary Materials. The scRNA-seq data reported in this paper have been deposited in the OMIX, China National Center for Bioinformatics/Beijing Institute of Genomics, Chinese Academy of Sciences (<https://ngdc.cncb.ac.cn/omix>; accession no. OMIX001061). The scRNA-seq data and relevant codes are publicly available in Zenodo (DOI: 10.5281/zenodo.7199080). The bulk RNA-seq data of brain tissues were downloaded from the GTEX database ([www.gtexportal.org/home/](http://www.gtexportal.org/home/)). The GEO database containing the PBMC single-cell sequencing dataset (GSM3892571) was downloaded as a control group to further characterize the functional characteristics of tumor-infiltrating immune cells. To reveal the molecular characteristics of the glial scar adjacent to the tumor tissue, the single-cell sequencing data (GSE119212) of eight brain tissues from the study of Zhong *et al.* were reanalyzed. The GSE118257 dataset was reanalyzed to characterize the oligodendrocyte lineage in this study. For the GSE118257 dataset, we retained the clustering information and mapped it to the generated UMAP plot and detected the expression of related genes.

Submitted 8 May 2022  
Accepted 10 March 2023  
Published 12 April 2023  
10.1126/sciadv.adc8933